Complex Phase Biasing of Silicon Mach-Zehnder Interferometer Modulators

by

Alex W. MacKay

A thesis submitted in conformity with the requirements
for the degree of Master of Applied Science
Graduate Department of Electrical and Computer Engineering
University of Toronto

Abstract

Complex Phase Biasing of Silicon Mach-Zehnder Interferometer Modulators

Alex W. MacKay
Master of Applied Science
Graduate Department of Electrical and Computer Engineering
University of Toronto
2014

A new any-point biasing scheme for Mach-Zehnder interferometer modulators which considers the complex phase is proposed. The Mach-Zehnder arm loss imbalance (imaginary part of the phase bias) is found by slightly perturbing the real and imaginary parts of the phase in each arm with low frequency pilot tones and monitoring and manipulating the spectral content at the output. This technique can be used to extend the possible extinction ratio, reduce the phase error, and better quantify the system chirp but also has some performance degradations which are also quantified and discussed. Simulation results indicate that the maximum extinction ratio of a typical modulator can be extended to $\gtrsim 40$ dB and maintained in the presence of ambient complex phase drift in the arms. Practical challenges for implementing this method with a silicon Mach-Zehnder modulator are discussed, but the analysis is general to other material platforms.

Acknowledgements

As a graduate student at the University of Toronto, I have benefited greatly from interacting with a wide variety of researchers both within and outside my field of study. I would like to thank all who have helped me develop during my time as a graduate student, but there are far too many to acknowledge individually. There are several people and organizations whose impact on myself and my research have been so great that I would like to address them personally.

First and foremost, I thank my research supervisor, Professor Joyce K. S. Poon, for her constant encouragement and motivation to look at problems in different ways. I thank my friends and colleagues: Hasitha Jayatilleka, Jared Mikkelsen, Wesley Sacher, Brett Kruger, and Benjamin Taylor for their support and valuable discussions. I thank Professor Lukas Chrostowski from the University of British Columbia and Dan Deptuck from CMC Microsystems for providing access to the silicon photonics foundry at the Institute for Microelectronics in Singapore through the SiEPIC program. I am grateful for funding provided by the National Sciences and Engineering Research Council of Canada (NSERC) as well as the Ontario Graduate Scholarship (OGS) program. Finally, I would like to thank my family for their ongoing love and support throughout my academic career.

Contents

List of Figures

List of Symbols

T	Power transmission of an MZI device
a_n	Total intrinsic field losses through both couplers and arm 'n' of an MZI
ϕ	Phase difference (real part) between the arms in an MZI, $\phi = \phi_1 - \phi_2$
ϕ_{bias}	Real part of the phase bias of an MZI
ϕ_s	Modulating signal (real part of the phase) of an MZM
ER	Extinction ratio
ER_M	Maximum (static) extinction ratio
γ	Field loss imbalance between arms in an MZI (a_2/a_1)
OMA	Optical Modulation Amplitude
Δf_c	Chirp: instantaneous frequency deviation
α_H	Henry (chirp) parameter
ϕ_m	Peak swing magnitude for ON-OFF keying signal
IL	Insertion loss
$\Re$	Responsivity of a photodiode (in A/W)
G_{TIA}	Transimpedance amplifier gain (in Ω)
V_{meas}	Measured voltage at MZM output after photodiode and amplification
$\mathrm{V}_{meas}(f)$	Spectral amplitude of the measured voltage signal at frequency f
θ	An electrical phase offset
$\theta_{filter}(f)$	Electrical phase response of a filter network
ϕ_r	Real part of optical phase shift ($\phi_r = \frac{2\pi n_{eff}}{\lambda} L$)
ϕ_i	Imaginary part of optical phase shift corresponding to optical loss
a_{nf}	Field loss in a waveguide (enumerated by n) containing a VOA
Δ_n	Applied DC intensity loss to a VOA in a waveguide (enumerated by n)
δ	Magnitude of a loss dither signal using a VOA
γ_{int}	Intrinsic field loss imbalance between arms in an MZI
γ_{tuned}	Average tuned field loss imbalance between arms in an MZI
$\Delta\phi_{drift}$	Drift in the real part of phase due to environmental fluctuations
$\Delta\alpha_{drift}$	Drift in loss due to environmental fluctuations
n_{eff}	Effective index of a waveguide
$\Delta\lambda_d$	Wavelength shift of a transmission spectral feature
$\Delta\lambda_{FSR}$	Wavelength free spectral range

List of Abbreviations

RoF	Radio-over-fiber
RF	Radio frequency
Rx	Receive or pertaining to the receiver end of a communication link
Tx	Transmit or pertaining to the transmitter end of a communication link
TIA	Transimpedance amplifier
EDFA	Erbium-doped fiber amplifier
SMF	Single mode fiber
C band	Conventional telecommunications wavelength band, $\lambda \in [1.53, 1.565]$ μm
BER	Bit-error-rate
Si	Silicon
SOI	Silicon-on-insulator
MZI	Mach-Zehnder Interferometer
MZM	Mach-Zehnder Modulator
MMI	Multi-mode interferometer
PAM	Pulse-amplitude modulation
BPSK	Binary phase-shift keying
DP-QPSK	Dual-polarization quadrature phase-shift keying
M-QAM	Quadrature amplitude modulation with 'M' symbols
DPMZM	Dual-parallel Mach-Zehnder modulator
OOK	ON-OFF keying
VOA	Variable optical attenuator
NRZ	Non-return-to-zero
LF	Low frequency
PD	Photodiode (or photodetector)
A/D	Analog-to-digital converter
D/A	Digital-to-analog converter
FFT	Fast Fourier transform
DSP	Digital signal processing
FPGA	Field-programmable gate array
PLL	Phase-locked loop
PRBS	Pseudo-random bit sequence

IME	Institute for Microelectronics
TWE	Travelling-wave electrode
CPW	Coplanar waveguide
CPS	Coplanar strips
TE	Transverse electric
TM	Transverse magnetic
FDTD	Finite-difference time-domain
VIA	Vertical interconnect access
FSR	Free spectral range

Chapter 1

Introduction

Over the past few decades, the way in which people and systems communicate has changed tremendously. For long-haul communications (> 1 km), there is a continually growing demand for higher capacity and higher bandwidth transmission networks due to the increased use of data-intensive activities online such as high-definition video streaming, social networking, and cloud-based storage and computing [1]. Optical communication systems provide the backbone of virtually all long-haul networks since the bandwidth potential exceeds that of any other available medium by several orders of magnitude [2, 3]. Additionally, the increased popularity of wireless devices such as cellphones over the past decade has led to more wide-spread applications for radio-over-fiber (RoF) technologies which use optical fibers to transport radio frequency (RF) carrier signals as well as the modulated information over long distances with antennas at either end of the fibers for receiving (Rx) and transmitting (Tx) the wireless signals [4, 5].

A simplified optical communication link is shown in Figure 1.1, where the grey boxes from left to right indicate the Tx, channel, and Rx respectively. Electrical devices in the link include the data source, transimpedance amplifier (TIA) and other electronic amplifiers or control circuits not shown. The passive optical devices make up the channel and include wavelength (de)-multiplexers (mux/demux) and optical waveguides to transport data on multiple carrier wavelengths. The (de)-multiplexers

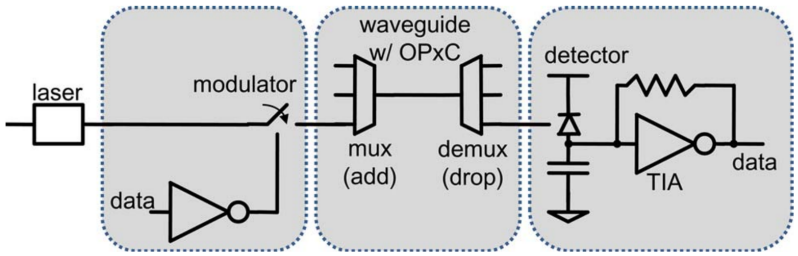

Figure 1.1: A generic simplified photonic link. Left to right shaded areas represent: Tx, channel, and Rx respectively. Clock and data recovery circuits and other control and amplifying stages not shown (taken from [6]).

are commonly implemented with arrayed waveguide gratings, planar concave diffraction gratings, interferometers, or resonant devices [7–10], while the waveguides are implemented with optical fibers to transport the data over long distances with low loss. The active optical devices include the laser and modulator at the Tx end, optical amplifiers in the channel (not shown), and the detector at the Rx end. To reduce size and costs, the Rx and Tx ends are often packaged together for transmitter-receivers and may include common circuitry for further cost reduction in transceivers.

Since the advent of commercially available optical amplifiers like erbium-doped fiber amplifiers (EDFAs) and Raman amplifiers, the main limiting factors of increasing aggregate bandwidth in long-haul systems are noise and dispersion in the channel, and related performance nonidealities at the Tx and Rx [2, 3, 11]. Long-haul networks use single-mode fiber (SMF) for communication channels since SMF has lower dispersion than multi-mode fiber in the conventional telecommunication band (C band, wavelength between 1.53 and 1.565 μm) where the optical losses are the lowest and most systems operate. SMF has a positive dispersion in the C band which leads to pulse broadening over large distances which can lead to intersymbol interference which can degrade the bit-error-rate (BER) in digital communication systems, especially at high data rates [11]. Since it is very expensive to replace existing optical fibers over long distances, most of the performance improvements in long-haul optical communication systems are enabled by advancements in performance and control of the Tx and control of the amplifiers in the channel. The focus of this work is to improve the performance of the most common type of modulator used in high speed transmitters,

the Mach-Zehnder modulator (MZM), using a new control technique to bias the complex phase. This work addresses design considerations for the implementation using a silicon photonic MZM, but the analysis is general. The motivation for this work and the choice of a silicon photonic implementation are given in the following sections.

1.1 Silicon Photonics

Silicon (Si) photonics, which uses silicon-on-insulator (SOI) as a substrate, is an attractive platform to make next generation optical communications transmitters and receivers. Si photonic circuits are cheap to fabricate due to decades of CMOS research and development, and the Si core is transparent across all common telecommunications wavelength bands so that photonic devices on SOI can easily be integrated into existing communication systems [12]. The SOI platform also provides a high refractive index contrast between the Si core ($n_{\mathrm{Si}} = 3.48$ at $\lambda = 1.55$ μm) and SiO_2 cladding ($n_{\mathrm{SiO_2}} = 1.44$ at $\lambda = 1.55$ μm) which allows for tight bends with low loss so that dense device integration is possible. For these reasons, the proposed work emphasises a silicon photonic implementation. A typical silicon photonics process platform showing the cross section of an SOI chip with common device structures, different material layers, and dimensions is given in Figure 1.2.

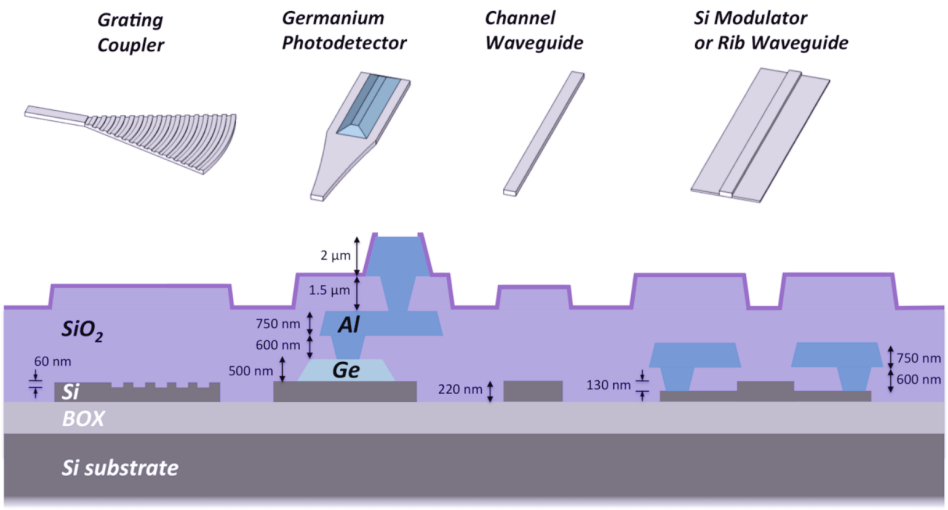

Figure 1.2: Silicon photonics platform from the A*STAR Institute for Microelectronics made available to researchers through OpSIS (taken from [13]). BOX refers to the buried oxide made of SiO_2.

1.1.1 Optical Modulators

One of the most important components in an optical communication system is an optical modulator which converts an electrical signal into the optical domain. The most common method to implement an optical modulator utilizes a Mach-Zehnder Interferometer (MZI) which converts a phase difference between its two arms to an intensity modulation as shown in Figure 1.3. Silicon has inversion symmetry and thus does not posses a linear electro-optic effect like lithium niobate, $LiNbO_3$, which is the most popular material for commercial Mach-Zehnder Modulators (MZMs). Instead, the refractive index is modulated by the carrier plasma dispersion effect [14]. A (PN or PIN) diode is integrated across the waveguide and can either inject carriers (forward bias) or deplete carriers (reverse bias) in the waveguide core to change the waveguide effective index [15, 16]. The modulator in Figure 1.3 uses multi-mode interferometers (MMIs) for the couplers but other coupler types are common [17–19]. The principle of operation and device geometry of the phase shifters in Figure 1.3 will be discussed in more detail in Chapter 4.

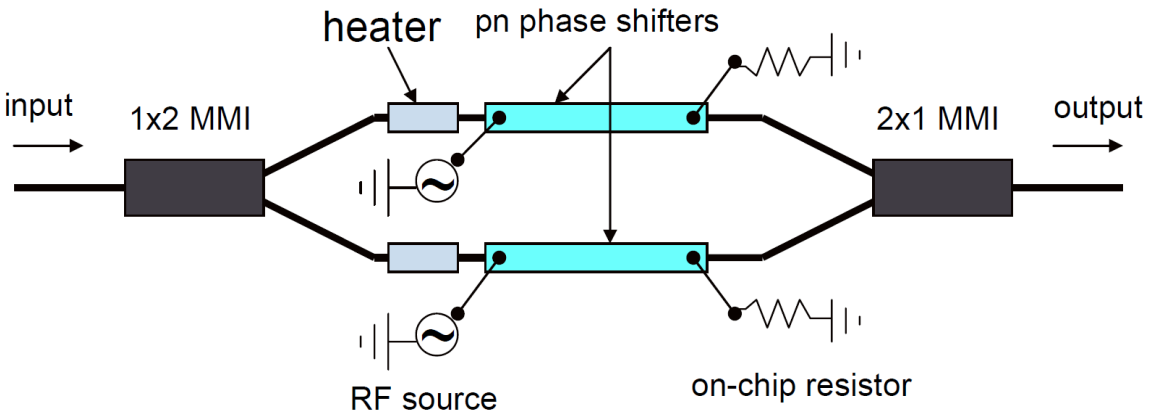

Figure 1.3: Mach-Zehnder modulator formed on the SOI platform (taken from [20]).

1.1.2 Modulator Biasing

For the best modulator performance, the modulator phase must be biased to an optimal operating point for a given application, as will be discussed more in Chapter 2. Additionally, the set bias point must be maintained using active feedback to

prevent drift due to thermal and other environmental variations with time [21, 22]. Silicon has a strong thermo-optic coefficient of $\frac{dn_r}{dT} \approx 1.8 \times 10^{-4}$ K^{-1} at $\lambda = 1.55$ μm [23] which makes it very susceptible to temperature dependent bias drift if the arms are not fabricated perfectly symmetrical or if there is a temperature gradient across the device. Similar ambient bias drifts occur in other types of modulators, and for this reason active modulator bias control systems are used in optical communication systems to ensure reliable performance [21]. Most bias control systems operate by constantly perturbing the MZM with a dither tone of known amplitude and frequency and monitoring the spectral content at the MZM output to determine the phase bias based on the MZM transfer function [21, 24–26]. The MZM transfer function is derived in Appendix A and given in Chapter 2 and a review of state-of-the-art phase biasing is given at the beginning of Chapter 3.

One issue with MZMs which has not been solved, is the inherent loss imbalance between the arms due to fabrication imperfections. This loss imbalance can be considered as a complex part of the optical phase (Chapter 3) which can reduce the extinction ratio (ER) which is the ratio between maximum and minimum output power, add phase error at the MZM output [27], and alter the frequency chirp which could be used to offset pulse broadening due to dispersion [28, 29]. All of these issues due to arm loss imbalance tend to degrade the transmitted signal fidelity as will be discussed more in Chapter 2. Current communication systems employ coherent detectors and advanced modulation formats that encode data onto both the amplitude and phase of the light. These systems are typically even more susceptible to impairments from the above limiting factors, with some modulation formats requiring better arm loss balance than can currently be reliably fabricated as will be discussed more in the next chapter [30]. Furthermore, any type of phase shifter in an MZM will adjust both the real and imaginary parts of the phase by the Kramers-Kronig relations, which means the loss imbalance of an MZM can be degraded by adjusting the real part of the phase bias. The effects of this for Si photonic phase shifters are discussed in Chapter 4. Tuning the MZM arm losses statically can improve the arm loss imbalance to

within less than 1% which improves all of the impairments mentioned above [31, 32]. The effects on the MZM performance of statically tuning the MZM arm losses are discussed in the next chapter. The performance effects due to MZM arm loss imbalance changing over time has not been studied since there is currently no method to monitor the loss imbalance during dynamic operation. This work proposes a method to monitor and tune the MZM arm loss imbalance, in addition to biasing the real part of the phase bias, during dynamic operation to improve the overall communication system performance.

1.2 Thesis Objectives

The purpose of this thesis is to extend the concept of modulator phase biasing and bias control to complex phase, with emphasis on MZMs used for digital communication. The real part of the phase is what is typically referred to as simply the "phase" while the imaginary part corresponds to the losses. In an MZI, the imaginary part of the phase bias corresponds to the loss imbalance between the arms. Balancing the MZM arm losses can improve the extinction ratio, phase error, and ability to estimate the modulator chirp which may have use in next-generation optical networks.

This dissertation also addresses practical issues in the implementation on SOI modulators. To observe these issues, measured data from a device designed to test this concept are studied. The power consumption of a complex phase biasing system was not investigated since it depends almost exclusively on the control circuitry used which varies significantly depending on factors such as device size, complexity, and cost requirements.

1.3 Thesis Organization

The organization of this thesis is as follows. Chapter 2 introduces a general system model for MZI devices and examines how several performance metrics of MZMs vary with different arm loss imbalances and how they can be improved with active tuning.

Chapter 3 introduces a new method to determine the loss imbalance and real phase difference between MZI arms simultaneously (complex phase bias) during dynamic operation. MATLAB simulation results of an MZM which actively measures and maintains the complex phase bias are given, and trade-offs to using this method are discussed. Chapter 4 discusses practical considerations and challenges to implementing the proposed complex phase biasing technique on an SOI MZM device and gives measured results from a circuit designed to achieve this functionality. Suggestions for improvements on a revised design are given throughout the chapter and future work on this topic is also addressed. Finally, Chapter 5 concludes this work by highlighting key achievements and subsequent work to be investigated.

Chapter 2

Loss Imbalance in MZMs: Performance Considerations

This chapter begins by presenting a simple time-dependent system model for an MZM applicable to other MZI-based devices, but the focus is on an MZM for digital modulation formats. The transfer function of a 1×1 MZM is analyzed and common bias points are introduced. The origin of loss imbalance between arms in an MZM, and its effects on performance metrics including extinction ratio, phase error, optical modulation amplitude, insertion loss, and chirp are examined and discussed.

2.1 Formalism: System Model of an MZM

A 1×1 MZM structure composed of a 1×2 coupler at the input followed by two delay lines with adjustable phase and a 2×1 coupler at the output is shown in Figure 2.1a. The input and output couplers can be formed using multi-mode interferometers, Y-branches, directional couplers or adiabatic couplers to provide precise splitting ratios [15, 17–19]. The phase shifters can be made from some combination of resistive heaters and/or diodes integrated into the waveguide in each arm of the MZM in silicon [16, 20]. The model here is general regardless of the type of couplers and phase shifters used but assumes that the phase shifters are ideal and do not vary the loss.

The system model of an MZM here treats the couplers and phase shifters as simple

signal lines and blocks characterized by loss and phase with respect to the electric field through each element[1]. Neglecting extraneous effects such as reflections and weak coupling with radiation caused at the input and output splitter/combiners, a 1×1 MZI structure can be modelled as a simple linear time-invariant (LTI) system as shown in Figure 2.1b. Figure 2.1b is color-coded in the same way as Figure 2.1a to show how the light is split into each arm (blue for arm 1 and pink for arm 2), phase shifted, and recombined at the output coupler. The tilde on the input and output fields denote the fact that they are phaser quantities (i.e. $\widetilde{\mathbf{E}} = \mathbf{E}e^{j\omega t}$). Definitions for all the terms appearing in blocks in the top arm of Figure 2.1b are given in Table 2.1. Similar definitions apply to all terms appearing in blocks in the bottom arm. The choice of nomenclature of the phase and loss subscripts (e.g. t and κ) is used only to maintain consistency with the 2×2 MZI in Appendix A.

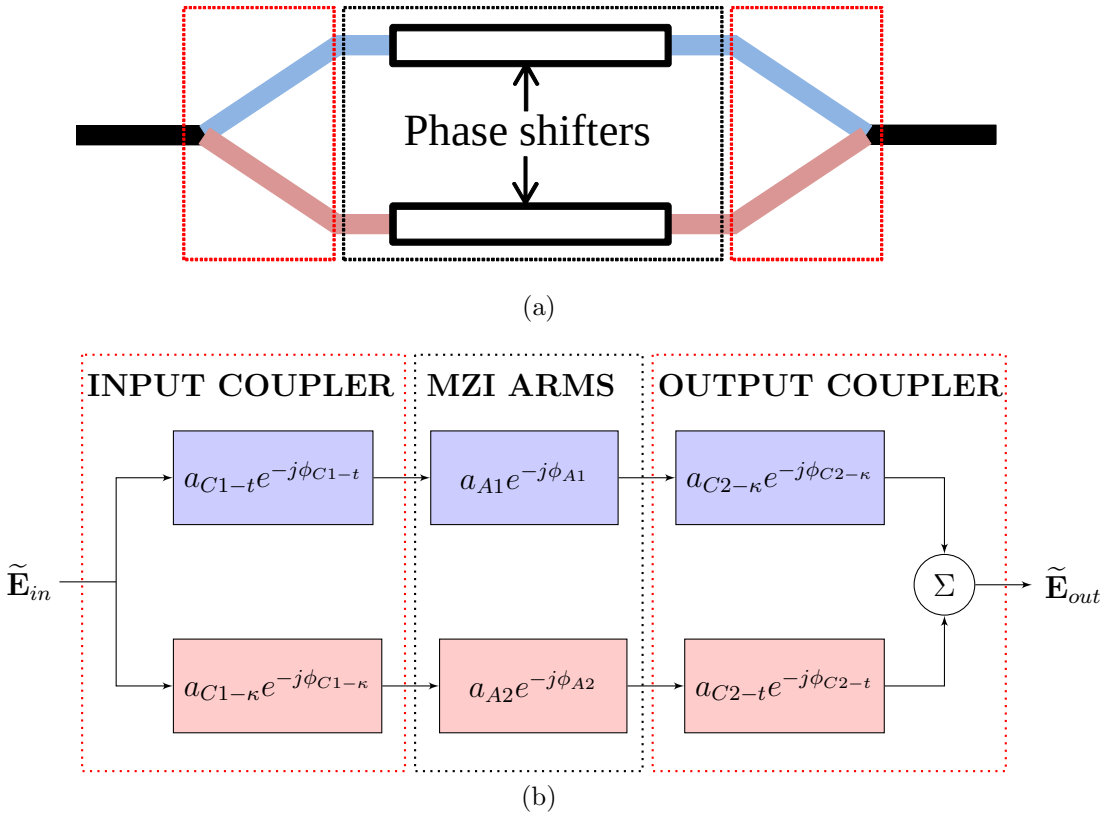

Figure 2.1: (a) Schematic and (b) block diagram of an MZM.

[1]A more precise derivation of the same relationship is given in Appendix A for a general 2×2 MZI which yields the same result at one of the output ports.

Table 2.1: System block diagram parameters

Paremeter	Description
a_{C1-t}	Field gain (loss) from the input coupler into arm 1
$a_{C2-\kappa}$	Field gain (loss) from arm 1 through the output coupler
a_{A1}	Field gain (loss) in arm 1
ϕ_{C1-t}	Phase induced from the input coupler into arm 1
$\phi_{C2-\kappa}$	Phase induced from arm 1 through the output coupler
ϕ_{A1}	Phase induced in arm 1

Without loss of generality, the system can be simplified by combining the field loss and phase shifts through each element of each arm as shown in Table 2.2. The output field is then a simple function of the input field given by

$$\widetilde{\mathbf{E}}_{out} = \widetilde{\mathbf{E}}_{in}\left(a_1 e^{-j\phi_1} + a_2 e^{-j\phi_2}\right). \tag{2.1}$$

Table 2.2: MZM field loss and phase in each arm

Paremeter	Definition	Description
a_1	$a_{C1-t}a_{A1}a_{C2-\kappa}$	Field gain (loss) through arm 1 and both couplers
a_2	$a_{C1-\kappa}a_{A2}a_{C2-t}$	Field gain (loss) through arm 2 and both couplers
ϕ_1	$\phi_{C1-t} + \phi_{A1} + \phi_{C2-\kappa}$	Phase induced through arm 1 and both couplers
ϕ_2	$\phi_{C1-\kappa} + \phi_{A2} + \phi_{C2-t}$	Phase induced through arm 2 and both couplers

Assuming there is no gain in the system, $(a_1 + a_2)^2 \leq 1$. The time-dependent transfer function for the light intensity (or power) using the slowly-varying envelope approximation (modulation frequency $\ll$ optical carrier frequency) is given by

$$T = \left|\frac{E_{out}}{E_{in}}\right|^2 = a_1^2 + a_2^2 + 2a_1 a_2 \cos\phi, \tag{2.2}$$

where ϕ is the phase difference between the arms, $\phi = \phi_1 - \phi_2$, and is generally a function of time. The phase difference is typically written as a sum of the DC bias and a modulating signal as $\phi = \phi_{bias} + \phi_s(t)$. For any type of amplitude modulation such as pulse-amplitude modulation (PAM), where a highly linear electro-optic conversion is desirable, it is most common to bias the phase at quadrature, $\phi_{bias} = \pm\frac{\pi}{2}$, since it is the most linear part of the transfer function. In some phase-shift keying modulation formats such as binary phase-shift keying (BPSK), it is common to bias at one of the nearly null points, $\phi_{bias} = \pm\pi$, since any phase swing centred about these points will produce approximately a π phase shift for $0 < \phi_{swing} \leq 2\pi$. This can be understood by considering Equation 2.1.

To ensure that the MZM can go to zero in the OFF state, $a_1 = a_2$. Any deviation from this ideal case is typically attributed to imperfect 50/50 couplers and much work is done to produce better couplers [33–36]. While even-splitting couplers are important, it is critical to emphasize that deviation from $a_1 = a_2$ can result from differences in the losses anywhere in the MZM arms, which may be due to fabrication imperfections, for example. Figure 2.2 shows an ideal transfer function (lossless with perfect splitting, $a_1 = a_2 = \frac{1}{2}$) with respect to the phase difference and highlights the common bias points.

2.1.1 Extinction Ratio, Phase Error, and Optical Modulation Amplitude

As mentioned in Section 1.1.2, the extinction ratio is defined as the ratio of the transmission in the ON state (T_{max}) to the transmission in the OFF state (T_{min}).

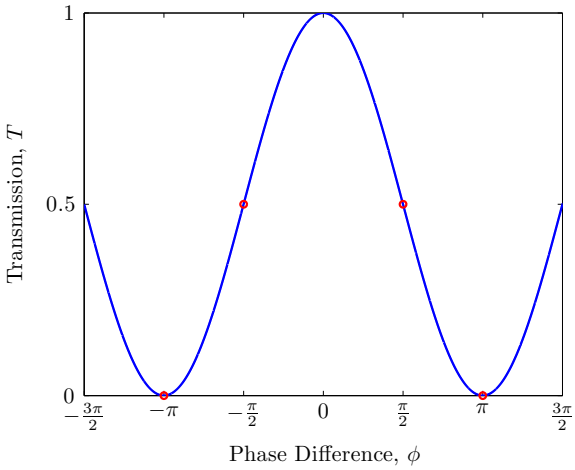

Figure 2.2: Ideal transfer function of an MZM with common bias points highlighted

This is usually referred to as the static extinction ratio since it is typically measured by varying a DC phase bias to one of the MZM arms to find the absolute maximum and minimum transmission. This is necessary since the dynamic extinction ratio (or just extinction ratio, ER) may be reduced when operating at high frequencies due to limited phase swings at high speeds or pulse shaping from the finite bandwidth of the electrodes. This will be discussed in more detail in the following chapters. Since this work warrants an alternative method to determine the "static" extinction ratio which can be done during dynamic operation, we will instead refer to this upper bound extinction ratio as the maximum extinction ratio, ER_M. Defining $\gamma = \frac{a_2}{a_1}$ as the field loss imbalance, the maximum extinction ratio can be expressed:

$$ER_M = \left(\frac{1+\gamma}{1-\gamma}\right)^2. \tag{2.3}$$

The (intensity) loss imbalance between the MZM arms is represented in the obvious way, as γ^2. MZMs which are considered well-balanced have $ER_M \gtrsim 20$ dB which is typically a lower limit for commercial high-frequency MZMs [37]. The lower limit of what is considered a "well-balanced" MZM corresponds to a loss imbalance of $\gamma^2 \approx 0.669$ which indicates that there is approximately 50% more power flowing through one arm than the other. In the case of some advanced modulation formats, the dynamic extinction ratio required to achieve a tolerable BER range can be limited by the maximum extinction ratio where some systems require $ER \gtrsim 40$ dB [27].

Current and next generation long-haul digital communication systems employ advanced modulation formats which can modulate both the intensity and phase of each carrier to improve spectral efficiency [3, 38]. Modern systems often use dual-polarization quadrature phase-shift keying (DP-QPSK) to achieve 100 Gb/s transmitters using symbol rates of 25 GBaud/s by only modulating the MZM output phase. Future systems operating at 400 Gb/s and beyond (without needing to increase symbol rates) will be realized using quadrature amplitude modulation with 'M' symbols (M-QAM) which improves spectral efficiency by encoding data onto both the amplitude and phase of optical carriers [39]. A single, high performance MZM with phase control in both arms can be employed to achieve any modulation format desired [40], but it is more common to use nested MZMs to simplify the driving signals and maintain control over the modulator chirp. As an example, a dual-parallel MZM (DPMZM) used for QPSK is given in Figure 2.3 to show how it can produce a constellation diagram with symbols in every quadrant by biasing the outer MZM at quadrature.

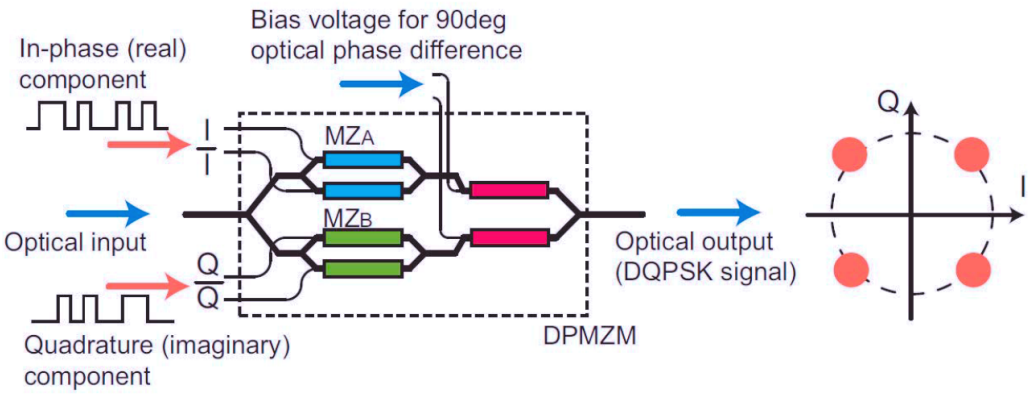

Figure 2.3: Schematic of a DPMZM used for QPSK Modulation (taken from [30]).

A loss imbalance in a single MZM can lead to a relative phase change at the output which differs from the balanced case which is problematic in modulation formats which encode data onto the optical phase. The MZM phase change at the output relative to the input can be derived from Equation 2.1 to be [28]

$$\phi_{out} = \tan^{-1}\left(\frac{\sin\phi_1 + \gamma\sin\phi_2}{\cos\phi_1 + \gamma\cos\phi_2}\right). \tag{2.4}$$

As communication networks adopt modulation formats with more bits per symbol, the maximum extinction ratio and corresponding phase error become more critical to system performance. As an example, it has been shown that using a DPMZM with $ER_M = 25$ dB for 256-QAM led to symbols near the origin appearing more than 50% the distance between neighbouring symbols [30]. This level of constellation distortion leads to a degraded BER which reduces the overall system performance.

Another modulator performance metric is the optical modulation amplitude (OMA) which is defined as the power amplitude difference between two symbols. In the case of ON-OFF keying (OOK), the OMA is the difference between the output power in the ON state (P_{ON}) and the power in the OFF state (P_{OFF}), $OMA = |P_{ON} - P_{OFF}|$. This is an important figure of merit, since it is often a direct indicator of the BER. As a simple example, for OOK assuming additive white Gaussian noise in both the ON and OFF states, the BER is given by [41]

$$\text{BER} = \frac{1}{2}\text{erfc}\left[\frac{OMA}{\sqrt{2}(\sigma_{ON} + \sigma_{OFF})}\right] \tag{2.5}$$

where erfc is the complementary error function and σ_{ON} and σ_{OFF} are the root-mean-square noise power in the ON and OFF states respectively. It is clear that having a large OMA will yield a lower BER. In long-haul communications, the modulator OMA is less critical than the extinction ratio since the signal is amplified at various points throughout each network.

2.1.2 Dispersion Issues: Chirp

One of the performance limiting factors in existing long-haul communication systems is fiber dispersion. One factor in modulators which can help or worsen the effects of dispersion is the chirp. Chirp is an instantaneous deviation in frequency given by $\Delta f_c = \frac{1}{2\pi}\frac{d\phi_{out}(t)}{dt}$ which is more commonly characterized by the Henry parameter [42]

$$\alpha_H = \frac{d\phi_{out}}{dt} 2P_{out}(t)\left[\frac{dP_{out}(t)}{dt}\right]^{-1} = 4\pi\Delta f_c(t)P_{out}(t)\left[\frac{dP_{out}(t)}{dt}\right]^{-1}, \tag{2.6}$$

where P_{out} is the modulator output power and ϕ_{out} is the relative phase change at the modulator output given in Equation 2.4. The output power can be found by multiplying the modulator input power by the transfer function in Equation 2.2, $P_{out} = P_{in}T$. From Equations 2.2, 2.4, and 2.6, we find [28]

$$\alpha_H = \frac{\phi_1' + \gamma^2\phi_2' + \gamma(\phi_1' + \phi_2')\cos(\phi_1 - \phi_2)}{-\gamma(\phi_1' - \phi_2')\sin(\phi_1 - \phi_2)}, \tag{2.7}$$

where α_H is generally a function of time and the prime indicates a derivative with respect to time.

It is common to characterize the chirp in the small signal regime so that α_H does not vary with time. If it is assumed that the phase change with respect to voltage is the same in both arms, the small signal Henry parameter when biased at quadrature in arm 2 ($\phi_{bias} = -\frac{\pi}{2}$) can be written as [28]

$$\alpha_{H-SS} = \frac{V_{\phi_{s,1}} + \gamma^2 V_{\phi_{s,2}}}{\gamma(V_{\phi_{s,1}} - V_{\phi_{s,2}})}, \tag{2.8}$$

where $V_{\phi_{s,1}}$ and $V_{\phi_{s,2}}$ are the voltage swings to the phase shifters in arm 1 and 2 respectively and typically have opposite polarity for push-pull modulation. A positive chirp ($\alpha_{H-SS} > 0$) leads to further pulse broadening than chirp free operation ($\alpha_{H-SS} = 0$), and a negative chirp ($\alpha_{H-SS} < 0$) can compress a pulse as it travels along a fiber. Controlled negative chirping of MZMs can thus be used to offset the effects of dispersion in long-haul communication networks [11, 29, 43]. Until [28], the analysis of the Henry parameter for MZMs neglected the loss imbalance γ and the small signal value was written as (the balanced case): $\alpha_{H-SS} = (V_{\phi_{s,1}} + V_{\phi_{s,2}})/(V_{\phi_{s,1}} - V_{\phi_{s,2}})$. This analysis is still common despite the fact that it was shown to wildly underestimate the chirp value using an MZM with an extinction ratio ≥ 12 dB, with errors of about 500% in the worst case [44]. Therefore, knowing the value of γ during dynamic operation can help improve network performance if controlled chirping is employed.

2.2 Biasing Losses

It is clear from the previous sections that imbalanced arm losses ($\gamma \neq 1$) in an MZM yields non-optimal performance since the extinction ratio is degraded and there is phase error at the output. Additionally, not knowing the value of γ is problematic if controlled chirping is necessary. For these reasons, it is proposed to bias the imaginary part of the phase (loss) in addition to the real part of the phase in MZMs to control the loss imbalance. The following sections address and discuss the pros and cons to static loss biasing in terms of the performance metrics highlighted.

2.2.1 Tradeoff between Extinction Ratio and Phase Error with Insertion Loss and Optical Modulation Amplitude

Actively tuning the arm losses (reducing a_1^2 or a_2^2) in an MZM can significantly improve the maximum extinction ratio, providing a greater available range for the dynamic extinction ratio. It has been experimentally demonstrated that using the nested MZIs in a DPMZM as variable optical attenuators (VOAs) can improve the extinction ratio of the main MZM from $ER_M \approx 30$ dB ($\gamma^2 = 0.881$) to $ER_{M,tuned} \gtrsim 70$ dB ($\gamma^2 = 0.999$) [31]. The loss imbalance can also be addressed by adding variable gain into the MZM arms using semiconductor optical amplifiers (SOAs) for example [45], but this is not viable in SOI, so we will not consider this. The practical implementation of VOAs will be discussed in Chapter 4 but below we assume that the losses can be varied independently from the real part of the phase by some means.

To quantify how much the dynamic extinction ratio in digital communication could be improved by tuning the losses, it is useful to examine how the extinction ratio changes with different phase swings. The simplest case to analyze is non-return-to-zero (NRZ) OOK. Recalling that the phase difference in Equation 2.2 can be written as $\phi = \phi_{bias} + \phi_s(t)$, for NRZ OOK [46]

$$\phi_s(t) = \sum_{k=1}^{N} \phi_k p(t - kT_b), \tag{2.9}$$

where $\phi_k = \pm\phi_m$ is the phase swing, $p(t)$ is the pulse shape, $T_b = \frac{1}{f_b}$ is the pulse length (bit period), and N is the sequence length. The pulse shape is assumed to be approximately the same in the ON and OFF states and have a normalized peak value. If the values of ϕ_{bias} and ϕ_m are chosen such that the maximum and minimum transmission points are not overshot, then the dynamic extinction ratio is

$$ER = \frac{1 + \gamma^2 + 2\gamma\cos\left(\phi_{bias} - \phi_m\right)}{1 + \gamma^2 + 2\gamma\cos\left(\phi_{bias} + \phi_m\right)}. \tag{2.10}$$

The swing which yields the maximum value of the extinction ratio, $\phi_m|_{ER_{max}}$, can be found by setting $\frac{\partial ER}{\partial \phi_m} = 0$, and is

$$\phi_m|_{ER_{max}} = \pi - \cos^{-1}\left[\frac{2\cos(\phi_{bias})}{\gamma + \frac{1}{\gamma}}\right] \approx \pi - \phi_{bias}, \quad \text{for } \gamma \approx 1. \tag{2.11}$$

Equation 2.10 with quadrature biasing and realistic "well-balanced" MZM arm imbalances is plotted in Figure 2.4 which shows that the phase swing, ϕ_m, needs to reach $\gtrsim 95\%$ of $\phi_m|_{ER_{max}}$ to have noticeable improvements ($\gtrsim 5$ dB) in the dynamic extinction ratio while adjusting γ. Typically the data signal modulating the MZM is amplified using high voltage drivers so that nearly full swings ($\phi_m \approx \phi_m|_{ER_{max}}$ for any ϕ_{bias}) are possible. The high ER condition of Equation 2.11 can always be met by adjusting ϕ_{bias} at the expense of a possible reduction in linearity or maximum output.

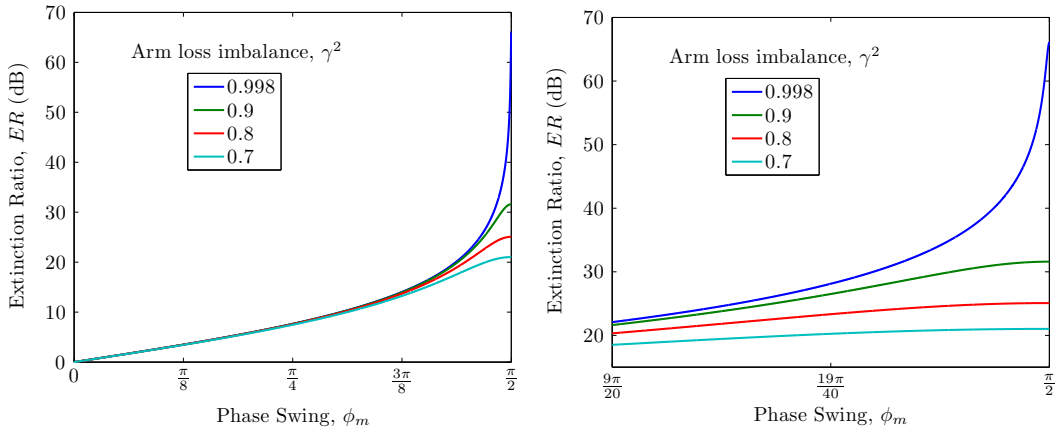

Figure 2.4: Extinction ratio as a function of phase swing and loss imbalance ($\phi_{bias} = \frac{\pi}{2}$) for phase swings in the range (a) $\phi_m \in [0, \phi_m|_{ER_{max}}]$, and (b) $\phi_m \in [0.9, 1] \times \phi_m|_{ER_{max}}$

The phase error due to imbalanced losses can be quantified as the difference between the relative phase shift at the output with what it would be in the balanced ($\gamma^2 = 1$) case: $\Delta\phi_{out} = \phi_{out} - \phi_{out}|_{\gamma^2=1}$. As an example, we consider phase shifting with balanced push-pull operation ($\phi_1 = -\phi_2$ for non-DC components). Figure 2.5 plots the phase error for balanced push-pull modulation with respect to the normalized output intensity amplitude.

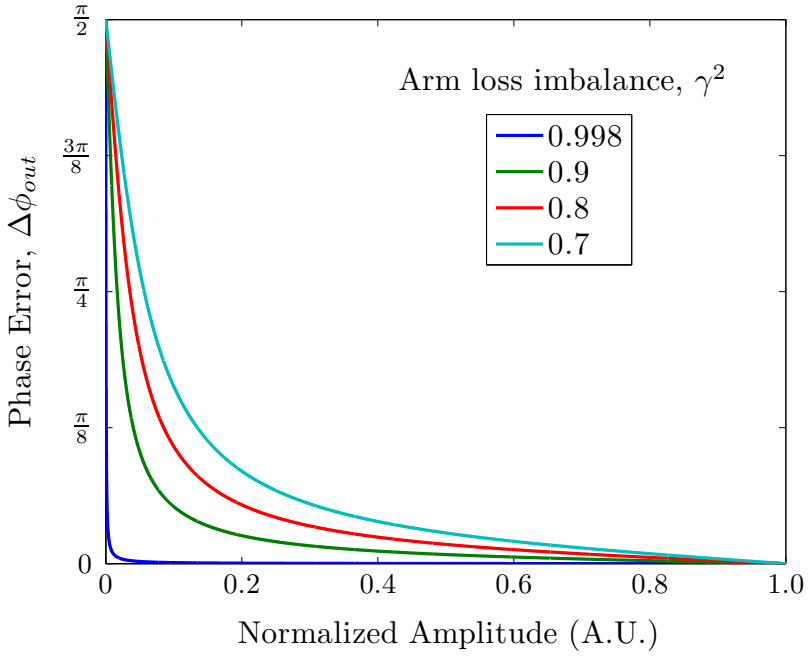

Figure 2.5: Phase error versus normalized transmission amplitude

From Figure 2.5, we see that balancing the MZM arm losses always improves the phase error for any normalized output transmission but is most significant for small output transmission. This indicates that M-QAM implemented in future systems will be affected much more significantly by arm loss imbalance than QPSK of current systems since M-QAM has constellation symbols with small normalized amplitude which also need precise phase control. These results are consistent with the constellation distortion observed in [27, 30], where it was suggested that M-QAM with large 'M' for advanced systems should have $ER_M \gtrsim 30$ dB for tolerable phase errors or $ER_M \gtrsim 40$ dB for negligible phase error.

While balancing the arm losses with VOAs shows improvement in the ER and phase error, there are also performance penalties. The device insertion loss (IL)

can be defined as the amount of power lost during maximum transmission and is typically expressed in dB: $IL = -10\log_{10} T_{max}$. When the losses are tuned such that $\gamma_{tuned} \geq \gamma_{int}$, where γ_{tuned} is the tuned loss imbalance and γ_{int} is the intrinsic loss imbalance, the change in insertion loss in dB is

$$\Delta IL \equiv IL|_{\gamma=\gamma_{tuned}} - IL|_{\gamma=\gamma_{int}} = 10\log_{10}\left[\frac{\gamma_{tuned}^2}{\gamma_{int}^2}\left(\frac{1+\gamma_{int}}{1+\gamma_{tuned}}\right)^2\right] \tag{2.12}$$

As a practical example, tuning the MZM intensity loss imbalance from 0.7 ($ER_M = 21$ dB) to 0.998 ($ER_M = 66$ dB) will incur an additional 0.8 dB of insertion loss. Tuning the arm loss imbalance can also have detrimental effects on the OMA. Assuming the real phase bias and swing remain unchanged and γ^2 is again increased, the tuned OMA for NRZ OOK is

$$OMA_{tuned} = \frac{\gamma_{int}}{\gamma_{tuned}} OMA_{int}, \tag{2.13}$$

where OMA_{tuned} is the OMA when $\gamma = \gamma_{tuned}$ and OMA_{int} is the OMA when $\gamma = \gamma_{int}$.

The negative effects on the insertion loss and OMA caused by loss tuning are generally not significant considering practical values but may be problematic in very sensitive, low energy per bit applications. In most long-haul communication networks, the optical signals are regularly amplified and thus all detrimental effects on OMA and IL can be dealt with at the expense of some incurred noise from the optical amplifiers. Furthermore, if the amplifiers are controlled to maintain constant maximum output power, a loss-balanced MZM ($\gamma^2 \approx 1$) will produce a larger OMA than the same MZM without tuning.

2.3 Summary

A system model for an MZM was presented, emphasizing the possible loss imbalance between the arms due to fabrication or design imperfections. Several key performance metrics including the maximum and dynamic extinction ratios, phase error, modulator chirp, insertion loss, and optical modulation amplitude were introduced and examined. We have shown that tuning the MZM arm losses can improve the extinction ratio, phase error, and the ability to estimate the chirp parameter at the expense of a small degradation in the insertion loss and optical modulation amplitude. These degraded parameters can be compensated by optical amplification after the modulator stage.

Chapter 3

Real-Time Complex Phase Biasing

This chapter begins by explaining the most prevalent method for biasing the real part of the phase in MZMs and expanding this concept to any-point biasing of the real part of the phase. Following that, a method to determine the complex phase bias (real part of phase bias and arm loss imbalance) of an MZM is developed. MATLAB simulation results of the complex phase biasing method are given and dynamic performance considerations and the extension to nested MZIs are discussed.

3.1 Review of Real Phase Bias Control

There are many proposed methods to control the real part of the phase bias in MZMs [24–26, 47, 48], but the most common methods all work on very similar principles [21]. In digital communication systems, the data signal, $\phi_s(t)$ is typically encoded using extra bits at the Tx end (for example 8b/10b encoding) to increase the transition frequency so that clock recovery is possible at the Rx end and to remove low frequency (LF) content to prevent baseline wander [11, 49]. There is a LF band which has no spectral content, which is utilized to determine the real part of the phase bias. Typically, a small amplitude, LF dither tone is superimposed onto the real part of the phase bias so that the real part of the MZM phase difference becomes

$$\phi = \phi_{bias} + \phi_d \cos(2\pi f_d t + \theta_d) + \phi_s(t), \tag{3.1}$$

where ϕ_d is the magnitude of the phase dither, f_d is the dither frequency, and θ_d is the electrical phase offset of the dither signal. The amplitude of the dither tone is chosen to be small enough that it can be detected at the MZM output without significant performance effects on the primary data signal. The phase dither usually ranges from less than 1% to about 5% of the phase swing, ϕ_m [21]. This dithering technique is used to perturb the system and determine an operating point of the transfer function by monitoring the spectral content at the MZM output. The first two LF spectral amplitudes of the transfer function (neglecting DC) due to the first two harmonics of the dither tone are:

$$|\mathrm{T}(f_d)| \ = 4a_1a_2|\sin(\phi_{bias})|J_1(\phi_d), \tag{3.2a}$$

$$|\mathrm{T}(2f_d)| = 4a_1a_2|\cos(\phi_{bias})|J_2(\phi_d), \tag{3.2b}$$

where $J_n(x)$ is an n^{th} order Bessel function of the first kind[1].

Usually a tap-off coupler is used at the MZM output so that the output signal can be monitored and a feedback loop to bias the phase can be implemented as shown in Figure 3.1. The tapped off power is converted to an electrical signal for processing. The power is converted to a voltage by going through a photodiode (PD) of responsivity $\mathfrak{R}$ (in A/W) followed by a TIA and filter network of passband gain G_{TIA} (in Ω) so that the measured voltage can be written as $V_{meas} = G_{TIA}\mathfrak{R}TP_{in}$. The filter network is either lowpass or bandpass. It is used as an anti-aliasing filter before digitizing the signal with an analog-to-digital converter (A/D) and can also be used to remove DC content to increase the available A/D resolution. The magnitude of the measured digital voltage is then directly proportional to the MZM optical output power in the LF passband assuming quantization error from the A/D can be neglected. The MZM LF spectral amplitudes as a voltage, $\mathrm{V}_{meas}(f)$, can be calculated using a fast Fourier transform (FFT) algorithm on some digital signal processing (DSP) circuit using a microcontroller, DSP chip, or field-programmable gate array (FPGA)

[1]These come from the use of the Jacobi-Anger identity during the Fourier expansion.

for example. After determining how to adjust the real phase, an updated bias is fed into the MZM through a digital-to-analog converter (D/A).

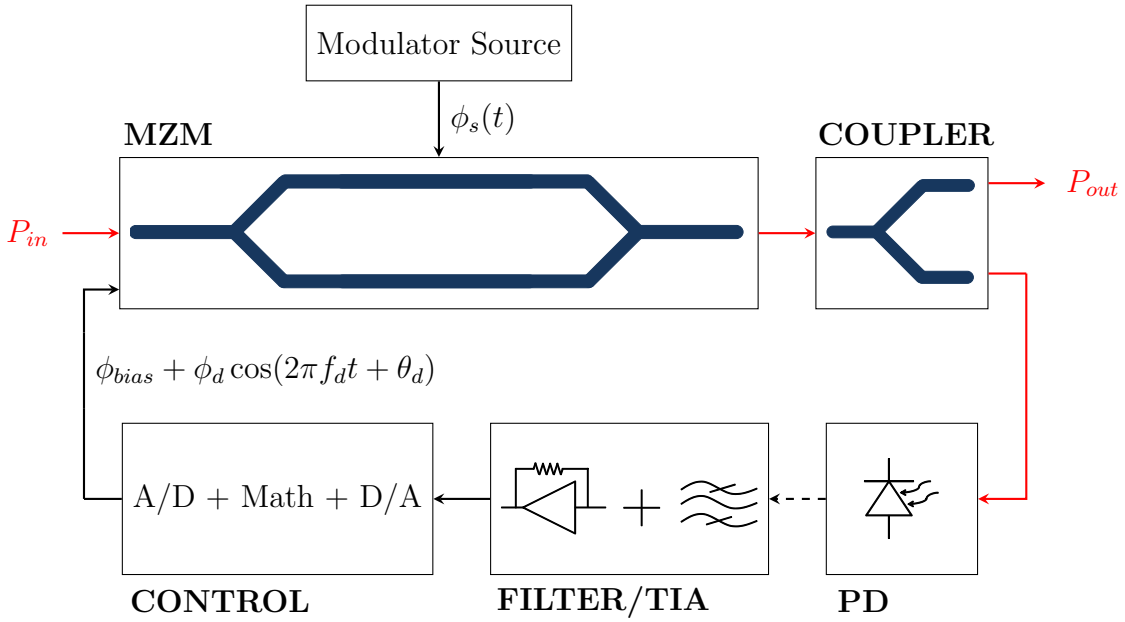

Figure 3.1: Feedback control circuit for any-point biasing of the real part of an MZM phase difference. Red and black paths are optical and electrical signals respectively. A dashed black path indicates an electrical current and a solid black path is a voltage.

The most common method of real phase bias locking recognizes that Equations 3.2a and 3.2b go to zero at the nearly null transmission ($\phi_{bias} = \pm\pi$) and quadrature ($\phi_{bias} = \pm\frac{\pi}{2}$) bias points respectively. Thus, by adjusting the phase bias and monitoring $\mathrm{V}_{meas}(f)$, it is straightforward to bias the real phase at these common operating points [21]. More recently, any-point phase biasing was realized by simply dividing Equations 3.2a and 3.2b [26, 50]:

$$\phi_{bias} = \tan^{-1}\left(\frac{\mathrm{V}_{meas}(f_d)}{\mathrm{V}_{meas}(2f_d)}\frac{J_2(\phi_d)}{J_1(\phi_d)}\right), \tag{3.3}$$

where we note that $\mathrm{V}_{meas}(f) = (G_{TIA}\Re P_{in})\mathrm{T}(f)$. This can be useful if a high extinction ratio is desired and a full swing is not possible as discussed in Section 2.2.1. It has been shown experimentally that this method is accurate in real phase bias locking to within less than $\pm 0.1°$ [26].

The problem with the above method is that it can only solve for ϕ_{bias} in the first quadrant (i.e. $\phi_{bias} \in [0, \frac{\pi}{2}]$) when just the magnitude of the spectral amplitudes

are used. In most practical situations, MZMs with equal arm lengths are used so the quadrant of ϕ_{bias} can typically be determined by the applied fields to each arm. However, this relation can be generalized to find $\phi_{bias} \in (-\pi, \pi]$ by considering the phase of the spectral amplitudes. We use a four-quadrant arctangent and define

$$\mathrm{V}_{meas}(f_d) = \begin{cases} |V_{meas}(f_d)|, & \text{if } \angle \mathrm{V}_{meas}(f_d) = \theta_d + \theta_{filter}(f_d) - \pi, \\ -|V_{meas}(f_d)|, & \text{if } \angle \mathrm{V}_{meas}(f_d) = \theta_d + \theta_{filter}(f_d), \end{cases} \tag{3.4a}$$

$$\mathrm{V}_{meas}(2f_d) = \begin{cases} |V_{meas}(2f_d)|, & \text{if } \angle \mathrm{V}_{meas}(f_d) = 2\theta_d + \theta_{filter}(2f_d), \\ -|V_{meas}(2f_d)|, & \text{if } \angle \mathrm{V}_{meas}(f_d) = 2\theta_d + \theta_{filter}(2f_d) - \pi, \end{cases} \tag{3.4b}$$

where $\theta_{filter}(f_d)$ and $\theta_{filter}(2f_d)$ are the electrical signal phase changes incurred in the system at frequencies f_d and $2f_d$ respectively. In this case, the electrical phase of the dithering tone as well as the (electrical) phase response of the feedback network at f_d and $2f_d$ must be approximately known. The electrical phase of the dithering tone can be known if it is controlled using a phase-locked-loop (PLL) and the electrical phase response of the system will be determined when designing the filters.

3.2 Realizing Complex Phase Bias Control

The method of phase biasing discussed so far will now be generalized to show how both the real and imaginary parts of the phase can be biased simultaneously. This section begins by introducing a DC and small signal model for VOAs which are necessary to adjust the imaginary part of the phase (loss). Thereafter we present an explanation of how complex phase biasing in an MZM can be achieved by independently dithering the real and imaginary parts of the optical phase in separate arms of the MZM.

3.2.1 Formalism: Variable Optical Attenuators

It is assumed that all optical waveguides used will have matched effective indices or adiabatic transitions between differing sections so that reflections can be ignored. In

this case, the electric field scattering parameters of any waveguide will be $S_{11} = S_{22} = 0$ and $S_{21} = S_{12} = e^{-\gamma_o L}$, where γ_o is the optical propagation constant and L is the waveguide length. We write the product $\gamma_o L$ as $j(\phi_r - j\phi_i)$, where ϕ_r is the real part of the phase and ϕ_i is the imaginary part of the phase corresponding to losses or gain. An ideal VOA has $\phi_i \geq 0$ which can be increased without affecting ϕ_r so that they can be analyzed independently. In a practical VOA, there will be an intrinsic loss (α_{int}) as well as the variable applied loss (α_{app}) which are separable: $\phi_i = \frac{\alpha_{int}+\alpha_{app}}{2}$. The attenuation of a waveguide containing a VOA is given by

$$a_{nf}^2 = e^{-\alpha_{int}} e^{-\alpha_{app}} = a_n^2 e^{-\alpha_{app}}, \tag{3.5}$$

where the f subscript indicates that the overall attenuation is now a function of some parameter (typically an applied voltage), n enumerates the waveguide, and a_n^2 is the intrinsic waveguide attenuation. If a small AC signal is applied to the VOA with attenuation amplitude δ and frequency f_L such that $\alpha_{app} = \alpha_{app,DC} + \delta\cos(2\pi f_L t)$, the VOA waveguide intensity and field losses can then be written ($\delta \ll 1$):

$$a_{nf}^2 \approx a_n^2 \Delta_n \left[1 - \delta\cos\left(2\pi f_L t\right)\right], \tag{3.6a}$$

$$a_{nf} \approx a_n \sqrt{\Delta_n} \left[1 - \frac{\delta}{2}\cos\left(2\pi f_L t\right)\right], \tag{3.6b}$$

where $\Delta_n = e^{-\alpha_{app,DC}}$ is the applied DC attenuation and $\alpha_{app,DC} \geq \delta$ since $\alpha_{app} \geq 0$.

3.2.2 Adding Loss Dithering to Determine Complex Phase

To tune the loss imbalance γ^2 of an MZM, the arms are designed to contain VOAs. Since it is unknown which arm in the MZM has more intrinsic loss, it is necessary to have a VOA in each arm. The transfer function in Equation 2.2 is modified to include these tunable losses to

$$T = a_{1f}^2 + a_{2f}^2 + 2a_{1f}a_{2f}\cos\phi. \tag{3.7}$$

Since the losses, a_{1f}^2 and a_{2f}^2, are now time-dependent in general, the loss imbalance γ^2 is also time-dependent. The effects of this variation with time will be addressed in Section 3.3.2. For the time being, we assume that any time-dependent variation of the losses can be treated as a small perturbation so that we can model the tuned field loss imbalance, γ_{tuned}, by the ratio of the average losses in each arm

$$\gamma_{tuned} = \frac{\langle a_{2f} \rangle}{\langle a_{1f} \rangle} = \frac{a_2}{a_1}\sqrt{\frac{\Delta_2}{\Delta_1}} = \gamma_{int}\sqrt{\frac{\Delta_2}{\Delta_1}}, \tag{3.8}$$

where γ_{int} is the intrinsic field loss imbalance and Δ_1 and Δ_2 are the applied DC attenuations to arm 1 and arm 2 respectively. The loss imbalance term represents the imaginary part of the phase bias, since from Equations 3.5 and 3.8, $\gamma_{tuned} = \left\langle e^{(\phi_{i,1}-\phi_{i,2})} \right\rangle$.

From Equation 3.2, we find there is not enough information to determine the loss imbalance by dithering the real part of the phase alone. We propose to dither both the losses and the real part of the phase independently and at different frequencies to determine both the real phase bias, ϕ_{bias}, and the loss imbalance, γ^2. This is the minimum number of perturbations (dither signals) necessary to completely characterize the complex phase bias. Dithering the loss alone in one arm will also not provide enough information to determine the loss imbalance. Dithering the loss in both arms independently could also provide the loss imbalance but leads to more complicated relations and would no longer provide the real part of the phase bias. We can choose to dither the loss in either arm, say arm 1 so that the field losses become

$$a_{1f} \approx a_1\sqrt{\Delta_1}\left[1 - \frac{\delta}{2}\cos\left(2\pi f_L t + \theta_L\right)\right], \tag{3.9a}$$

$$a_{2f} \approx a_2\sqrt{\Delta_2}, \tag{3.9b}$$

where δ is now the magnitude of the loss dither, f_L is the loss dithering frequency, and θ_L is the electrical phase offset of the loss dither signal. A system-level schematic of an MZM with separate sections for the real phase biasing, loss biasing, and data signals (modulation of the real part of the phase) is shown in Figure 3.2.

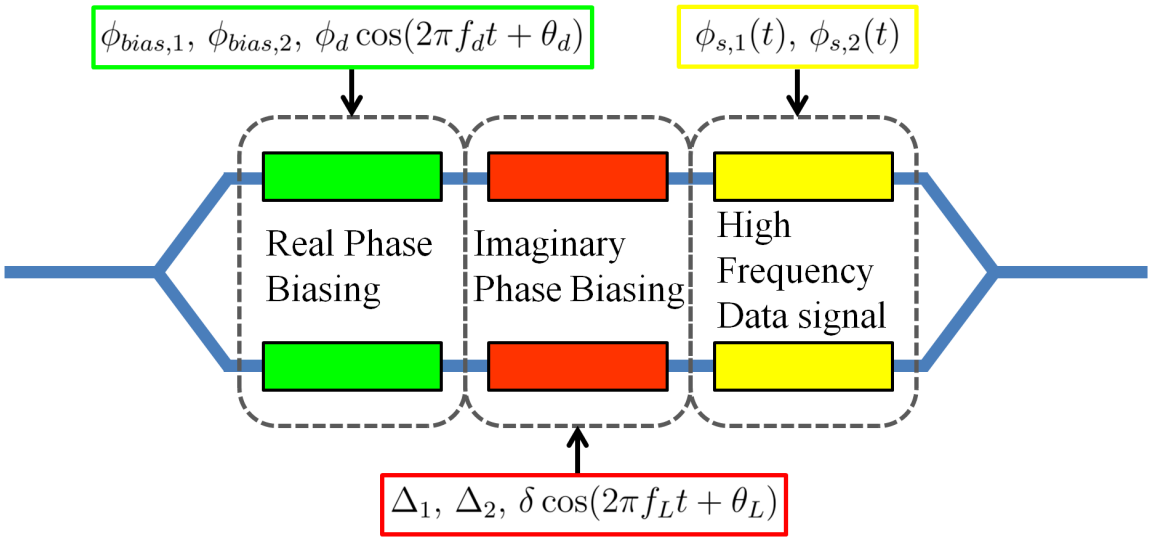

Figure 3.2: System-level schematic of an MZM used for complex phase biasing and modulation, having separate sections for real phase biasing, imaginary phase biasing, and modulation. Input signals are marked with arrows pointing toward the schematic and the subscripts 1 and 2 on each signal indicates which arm it is applied to.

From Equations 3.7 and 3.9, the spectral amplitudes at f_d and $2f_d$ (equation 3.2) only change by the applied DC attenuation ($a_1 \to a_1\sqrt{\Delta_1}$ and $a_2 \to a_2\sqrt{\Delta_2}$) and the spectral amplitude of the optical transmission at the loss dithered frequency is

$$|\mathrm{T}(f_L)| = |a_1^2\delta\Delta_1 + a_1a_2\delta\sqrt{\Delta_1\Delta_2}\cos(\phi_{bias})J_0(\phi_d)|. \tag{3.10}$$

There are other LF spectral features due to mixing of the f_d and f_L tones and their harmonics which may be in the frequency band of interest (i.e. where we are calculating the FFT; below the anti-aliasing filter cutoff frequency) depending on the choice of f_d and f_L. However, for small ϕ_d and δ these spectral amplitudes become negligibly small and are also unnecessary to consider when determining the complex phase bias. The real part of the phase bias can still be found using Equation 3.3, and once it is known, the loss imbalance can be found by solving Equations 3.10 and 3.2 to give

$$\gamma_{tuned}^{-1} = \frac{4J_1(\phi_d)}{\delta}\frac{\mathrm{V}_{meas}(f_L)}{\mathrm{V}_{meas}(f_d)}\sin(\phi_{bias}) - J_0(\phi_d)\cos(\phi_{bias}), \tag{3.11a}$$

$$\gamma_{tuned}^{-1} = \left[\frac{4J_2(\phi_d)}{\delta}\frac{\mathrm{V}_{meas}(f_L)}{\mathrm{V}_{meas}(2f_d)} - J_0(\phi_d)\right]\cos(\phi_{bias}), \tag{3.11b}$$

where $\mathrm{V}_{meas}(f_d)$ and $\mathrm{V}_{meas}(2f_d)$ are as they were defined in Equation 3.4 and

$$\mathrm{V}_{meas}(f_L) = \begin{cases} |V_{meas}(f_L)|, & \text{if } \angle \mathrm{V}_{meas}(f_d) = \theta_L + \theta_{filter}(f_L) - \pi, \\ -|V_{meas}(f_L)|, & \text{if } \angle \mathrm{V}_{meas}(f_d) = \theta_L + \theta_{filter}(f_L). \end{cases} \tag{3.12}$$

Since ϕ_d, δ, Δ_1, Δ_2, θ_L, θ_d, and $\theta_{filter}(f)$ are all known values, Equations 3.3 and 3.11 can be solved to determine the complex phase bias (ϕ_{bias} and γ) dynamically. It is important to note that γ_{tuned} is expressed as an inverted value in Equation 3.11 only because of the definition given in Equation 3.8 and that we chose to dither the losses in arm 1. As a result, γ_{tuned} can be greater than or less than 1 to determine which arm has more loss and by how much relative to the other arm.

Equations 3.11a and 3.11b are equally valid in general, but in practice one would be better suited to the bias chosen since $\mathrm{V}_{meas}(f_d) \to 0$ for $\phi_{bias} \approx \pm\pi$ and $\mathrm{V}_{meas}(2f_d) \to 0$ for $\phi_{bias} \approx \pm\frac{\pi}{2}$. For this reason, ϕ_{bias} should first be calculated using Equation 3.3 to determine whether Equation 3.11a or 3.11b should be used to calculate γ_{tuned}. This is discussed more in the following section.

3.2.3 Determining Operating Parameters

The previous section has shown that the complex phase bias can be determined by dithering the real and imaginary parts of the phase, but the values of ϕ_d, δ, f_d, and f_L were given little attention. The magnitude of ϕ_d and δ should be kept to a minimum to ensure performance is not degraded significantly from these perturbing signals as will be discussed in more detail in Section 3.3.2. It was mentioned in Section 3.1 that ϕ_d is typically less than 1% to 5% of ϕ_m, which is sufficient for the second harmonic from the real phase dither signal to be detected with high resolution at the output. Since the limiting signal to detect is the second harmonic from the real phase dithered signal, a lower bound for δ can be found by setting $|\mathrm{T}(f_L)|_{max} = |\mathrm{T}(2f_d)|_{max}$. To simplify the relation, it is assumed that $a_1 \approx a_2$ and $\Delta_1 \approx \Delta_2$ and the Bessel functions are approximated by their second order expansions. The lower bound on δ to ensure $\mathrm{V}_{meas}(f_L)$ is detectable with good resolution is given by

$$\delta_{min} = \frac{2\phi_d^2}{8 - \phi_d^2}. \tag{3.13}$$

As a practical example, for $\phi_d = 0.01\frac{\pi}{2}$, the minimum loss dither would be $\delta_{min} \approx 6.2 \times 10^{-5}$ which corresponds to a loss swing of less than 0.001 dB. In practice, the minimum achievable δ will be limited by the D/A resolution and transfer function of the VOA. In this analysis, we will assume that the combined D/A and VOA resolution will be limited to 0.05 dB ($\delta \approx 0.012$). This is still a fairly high resolution, but is achievable as will be discussed in Chapter 4.

The frequencies f_L and f_d are chosen such that the dithering tones do not interfere with the primary data signal or each other at any of their harmonics of interest. It is also desirable to choose frequencies which are well below the sampling frequency of low cost A/Ds so that this method of complex phase biasing can be implemented with a cost effective system. Typical values of f_d are on the order of 1 kHz [21]. In the analysis here we will choose $f_d = 1$ kHz and $f_L = 2.4$ kHz.

To determine whether Equation 3.11a or 3.11b should be used, the magnitudes of $\mathrm{V}_{meas}(f_d)$ and $\mathrm{V}_{meas}(2f_d)$ are compared. The spectral amplitude which is larger determines which equation to use, since it will provide better A/D resolution. Comparing Equations 3.2a and 3.2b, we find that using Equation 3.11a is preferable for most values of ϕ_{bias} when ϕ_d is small. We define the regime for the real part of the phase bias where Equation 3.11b is preferable to use as $\phi_{bias}|_{\text{eq.b}}$. Using a second order expansion for the Bessel functions,

$$m\pi - \tan^{-1}\left(\frac{\phi_d}{4}\right) \lesssim \phi_{bias}|_{\text{eq.b}} \lesssim m\pi + \tan^{-1}\left(\frac{\phi_d}{4}\right). \tag{3.14}$$

For example, if $\phi_d = 0.01\frac{\pi}{2}$, the range of the real part of the phase bias where equation 3.11b should be used is: $\pi(m - 1.25 \times 10^{-3}) \lesssim \phi_{bias}|_{\text{eq.b}} \lesssim \pi(m + 1.25 \times 10^{-3})$.

3.3 Simulation and Verification

To verify that the relations from the previous section can determine and lock the complex phase bias during dynamic operation, the system was modelled using MATLAB. A simplified block diagram schematic of the system model is given in Figure 3.3. All intrinsic and applied phase shifts were modelled using their exponent relations (see MZM model block in Figure 3.3) without small signal approximations. The phase shifters and VOAs were assumed to have a linear response with respect to an applied voltage so that the loss and real part of the phase could be varied directly to simplify the feedback analysis.

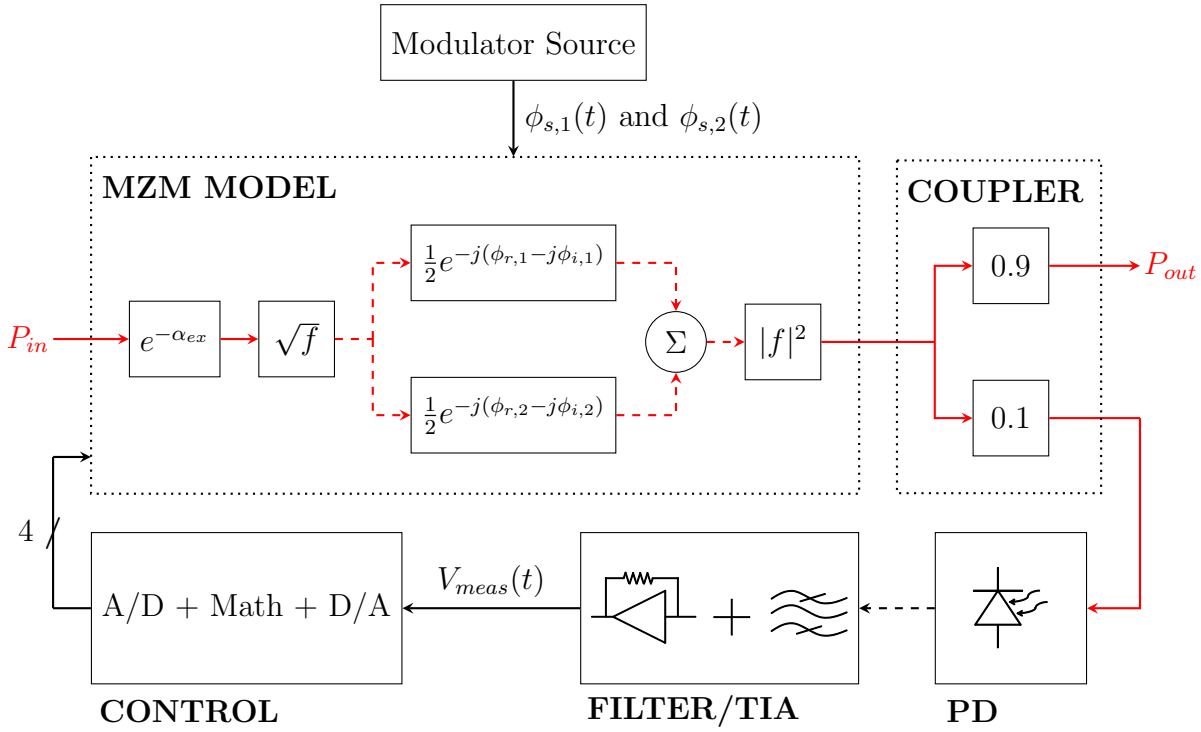

Figure 3.3: Simplified system model of MZM with complex bias control implemented in MATLAB. Solid and dashed red lines indicate optical intensity and an optical field respectively. Solid and dashed black lines indicate electrical voltage and current respectively. The output of the control block contains the dithering and biasing signals for the real and imaginary parts of the MZM phase. The f in the square root and squaring blocks indicates the input function into each block.

The real and imaginary phase components of the MZM arms during dynamic operation are a superposition of the biasing and dithering signals from the control circuit, the modulating signal from the modulation source, and any possible time-

dependent drifting due to environmental factors such as thermal fluctuations. To remain consistent with the previous analysis, the losses were dithered in arm 1 only and the real part of the phase was dithered independently in arm 2. The complex phase in each arm is then given by

$$\phi_{r,1} = \phi_{bias,1} + \Delta\phi_{drift,1}(t) + \phi_{s,1}(t), \tag{3.15a}$$

$$\phi_{r,2} = \phi_{bias,2} + \Delta\phi_{drift,2}(t) + \phi_{s,2}(t) + \phi_d \cos(2\pi f_d t + \theta_d), \tag{3.15b}$$

$$\phi_{i,1} = \frac{\alpha_{app,1}}{2} + \frac{1}{2}\Delta\alpha_{drift,1}(t) + \frac{\delta}{2}\cos(2\pi f_L t + \theta_L), \tag{3.15c}$$

$$\phi_{i,2} = \frac{\alpha_{app,2}}{2} + \frac{1}{2}\Delta\alpha_{drift,2}(t), \tag{3.15d}$$

where $\Delta\phi_{drift,1}(t)$ and $\Delta\phi_{drift,2}(t)$ are the ambient drifts in the real part of the phase in arms 1 and 2 respectively, and $\Delta\alpha_{drift,1}(t)$ and $\Delta\alpha_{drift,2}(t)$ are the ambient drifts in the loss in arms 1 and 2 respectively.

The input power, P_{in}, was set to 10 dBm (10 mW) and a 10% tap-off coupler was used at the MZM output for the feedback biasing circuit. The excess optical loss in the system was characterized by α_{ex} which can be from coupling losses to an external laser or common waveguide losses in the arms for example. The excess loss was set to 5 dB based on experimental data in Chapter 4. The system was tested for OOK modulation using a $2^{11}-1$ long pseudo-random bit sequence (PRBS) modulator source in balanced push-pull operation ($\phi_{s,1}(t) = -\phi_{s,2}(t)$). The PD responsivity used was $\mathfrak{R} = 0.75$ A/W which is typical for recent germanium PDs operating near $\lambda = 1.55$ μm [17, 51]. The bandpass filter and TIA was modelled with a Chebyshev type II filter with a realistic gain of $G_{TIA} = 250$ kΩ, cutoff frequencies of 500 Hz and 3 kHz, and a 70 dB stopband rejection. After filtering, the sequence was sampled at $F_s = 8192$ Sa/s and buffered in segments of length $N = 1024$ for DSP and control.

3.3.1 Automated Complex Phase Bias Determination and Locking

The basic algorithm for real-time complex phase bias locking is given in Figure 3.4.

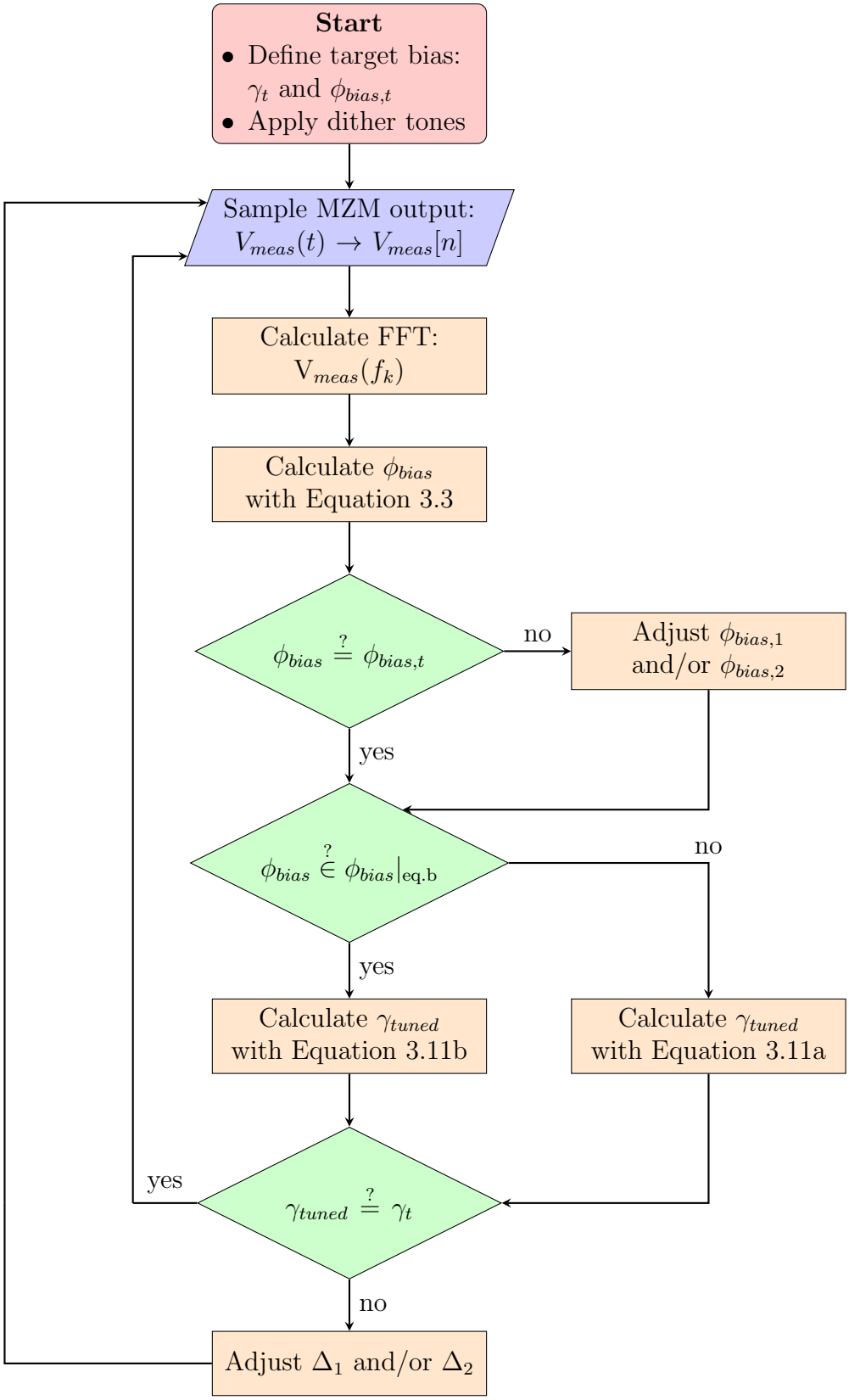

Figure 3.4: Flow chart of the basic algorithm to set and lock the complex phase bias of an MZM or other MZI device.

To observe the A/D resolution required and if quantization needs to be considered, the LF FFT magnitude spectrum for two different real phase bias points and loss dither magnitudes are shown in Figure 3.5. Figure 3.5a uses the corner case conditions of Equations 3.13 and 3.14, which is not a practical operating point, but it clearly shows the important spectral features and the small magnitude of the second harmonic of the real phase dithering signal. The low spectral content at $2f_d$ is the limiting component for the A/D performance and it is clear from Figure 3.5a that a sub-mV resolution is necessary. We will assume that quantization error can be neglected since bipolar A/Ds with resolution of tens of μV and smaller are available [52] and the TIA gain could also be increased if necessary.

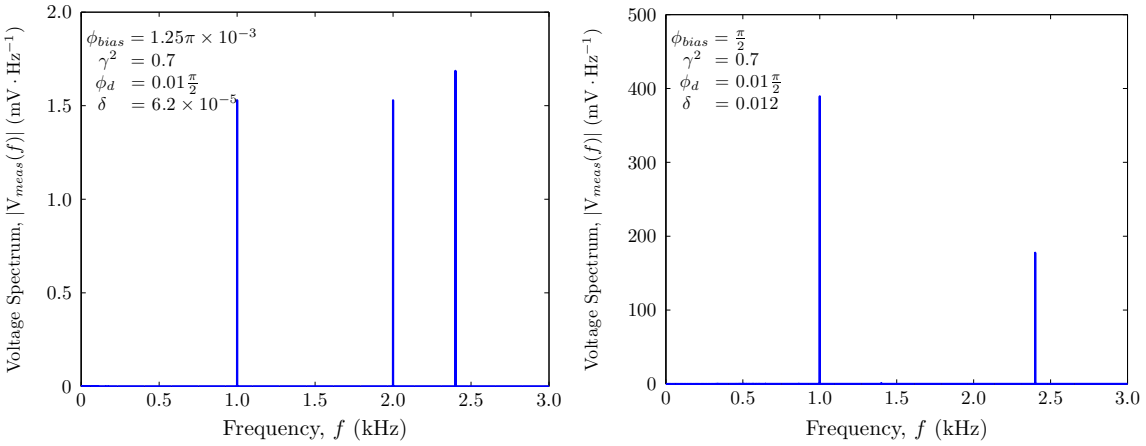

Figure 3.5: FFT spectrum with operating parameters annotated on the graphs at (a) an impractical operating point which clearly shows all important spectral features, and (b) quadrature biasing with realistic phase and loss dither signals

In a practical implementation of this system, the digital control would likely be performed on a low cost embedded device with limited memory and mathematical capability. For this reason, the Bessel functions of Equation 3.11 are approximated up to their second order expansion terms for calculation. The system in Figure 3.3 was simulated at various complex phase bias points over the range $\gamma^2 = [0.6, 0.7, 0.8, 0.9, 0.95, 0.998]$ and $\phi_{bias} \in [-\frac{3\pi}{4}, \pi]$ in increments of $\frac{\pi}{4}$, and the calculated complex phase bias points are plotted in Figure 3.6. It was found that the worst case errors calculating ϕ_{bias} and γ^2 were less than 0.05% and 0.15% respectively.

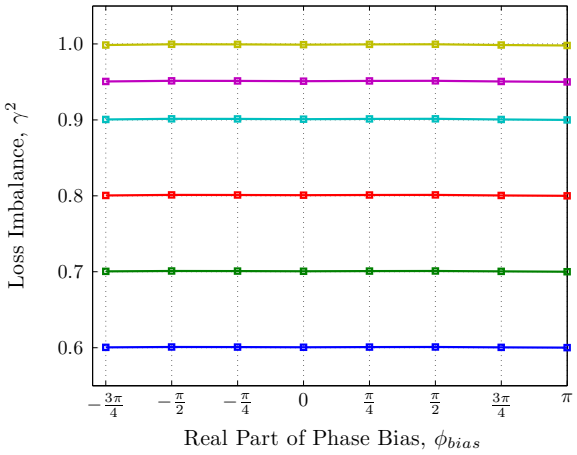

Figure 3.6: Calculated values of complex phase bias with $\phi_d = 0.01\frac{\pi}{2}$ and $\delta = 0.012$ over the range of $\gamma^2 = [0.6, 0.7, 0.8, 0.9, 0.95, 0.998]$ and $\phi_{bias} \in [-\frac{3\pi}{4}, \pi]$ in increments of $\frac{\pi}{4}$. The largest errors for calculated values were $< 0.05\%$ and $< 0.15\%$ for ϕ_{bias} and γ^2 respectively.

The ambient drift in the real part of the phase bias usually becomes significant over periods on the order of minutes or longer due to thermal fluctuations or other environmental factors, but the drift of loss imbalance over time has not been investigated. In a real MZM, the method of optimizing the real and imaginary parts of the phase bias to a target operating point will vary based on how much is known about the VOA and real phase shifter transfer functions. Since the given model assumes linear transfer functions with respect to voltage for both the real phase shifters and VOAs, the complex phase bias can be immediately adjusted to the correct operating point after each FFT calculation.

To test the functionality of the feedback control system with environmental fluctuations, random complex phase drifts are applied to the MZM over two minutes as shown in Figure 3.7. In this simulation, the MZM is modulated with balanced push-pull OOK with a maximum phase swing of $\phi_m = 0.48\pi$ at RF. To achieve a high extinction ratio and minimum output phase error, the optimal complex phase bias is then $\phi_{bias} = 0.52\pi$ (Equation 2.11) and $\gamma^2 = 1$. The intrinsic loss imbalance is $\gamma^2 = 0.7$ and ϕ_{bias} is set correctly before drifting. The maximum insertion loss penalty using active feedback for this test scenario is about 1 dB. Figure 3.7c shows that a higher extinction ratio can be obtained using this complex phase locking method.

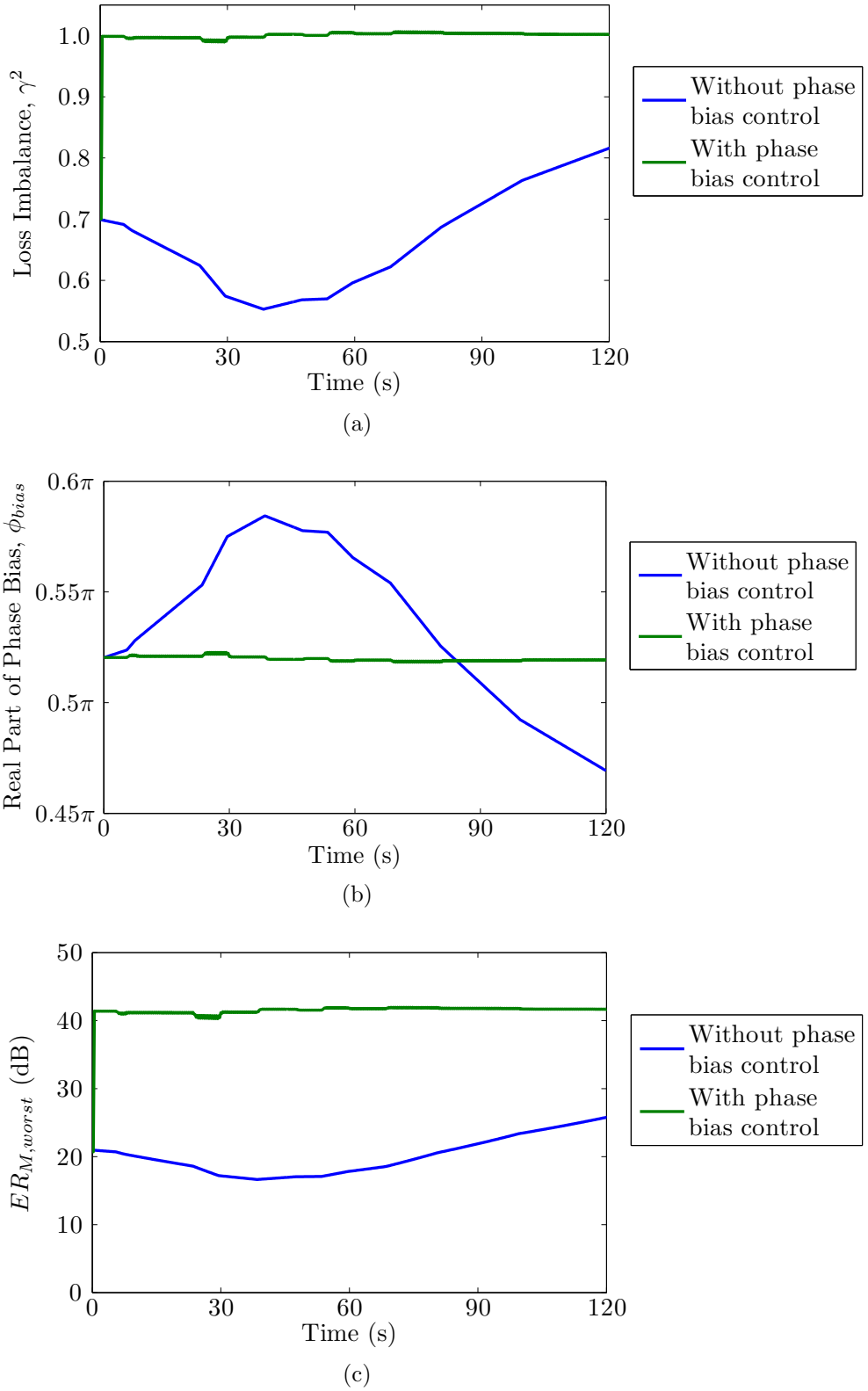

Figure 3.7: Simulation results of the (a) intensity loss imbalance, (b) real part of the phase bias, and (c) worst case extinction ratio for an MZM with drifting complex phase bias. The green line indicates the parameter values obtained when active complex phase locking is employed and the blue line is for an uncontrolled MZM.

3.3.2 Dynamic Effects on Performance

Until now, the time variation of the loss imbalance due to loss dithering was neglected and γ was treated as a constant. The time-dependent field loss imbalance is

$$\gamma(t) = \gamma_{tuned} e^{-\delta/2\cos(2\pi f_L t + \theta_L)} \approx \gamma_{int}\sqrt{\frac{\Delta_2}{\Delta_1}}\left(1 - \frac{\delta}{2}\cos(2\pi f_L t + \theta_L)\right). \tag{3.16}$$

For $\delta \ll \gamma_{tuned}^2$, the time variation of γ does not significantly affect the MZM output phase (Equation 2.4) and thus it can still be treated as a small perturbation on a nearly constant phase. Similarly, since f_L is much smaller than the bit rate f_B (modulation frequency), and since the output phase does not change significantly, the time-dependent effects on the chirp due to loss dithering can also be neglected.

One metric which can be noticeably affected by the time-dependent variation of the loss imbalance is the insertion loss. When the arm losses are approximately balanced, the change in insertion loss due to dithering is (in dB)

$$\Delta IL_L(t) \approx 2.17\delta\cos(2\pi f_L t + \theta_L - \pi). \tag{3.17}$$

This varying loss can easily be compensated using a controlled optical amplifier after the Tx stage. There is also a tradeoff for the dynamic extinction ratio using this complex phase biasing method. The extinction ratio can be improved by compensating for the loss imbalance but will ultimately be limited by the loss dithering in the OFF state which cannot be compensated during dynamic operation. To see the extinction ratio improvement and its limitations more clearly, the MATLAB system model was modulated using OOK to produce eye patterns shown in Figure 3.8 for two different intrinsically loss imbalanced MZMs without compensation, and one which uses complex phase biasing to obtain $\gamma_{tuned}^2 \approx 1$. The model was simulated using balanced push-pull modulation with a 10 Gb/s PRBS $2^{11}-1$ signal having $\phi_{bias} = 0.52\pi$ and $\phi_m = 0.48\pi$. To add pulse shaping, a 30 GHz lowpass filter was applied at the modulator but no other practical bandwidth limitations were imposed on the system.

The extinction ratio of an OOK modulator is typically defined by the ratio of the

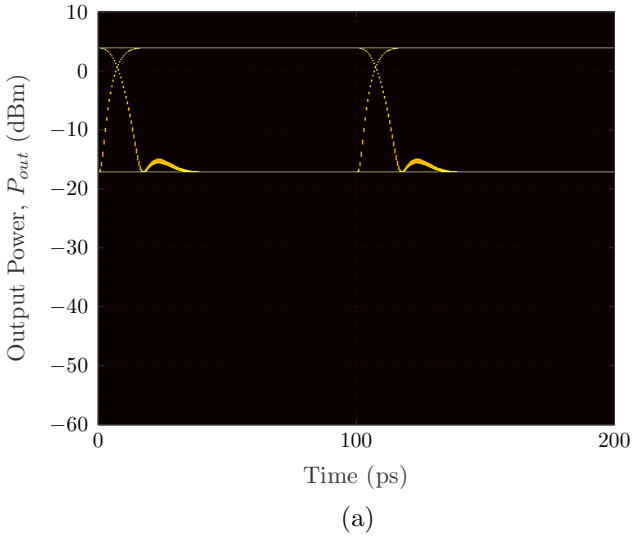

(a)

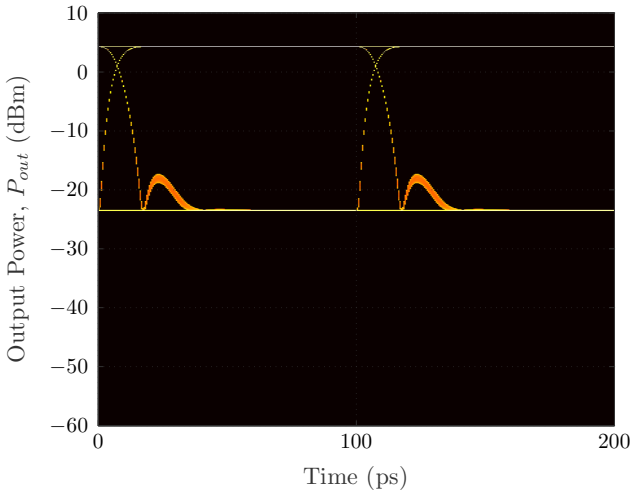

(b)

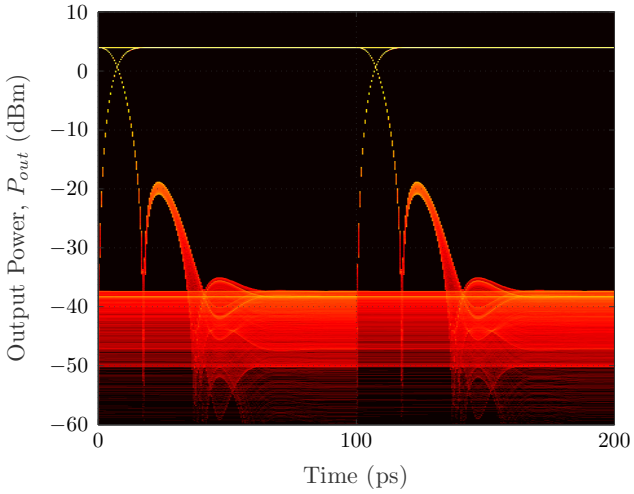

(c)

Figure 3.8: Eye patterns of OOK modulation for (a) $\gamma^2 \approx 0.7$ (no loss balancing), (b) $\gamma^2 \approx 0.85$ (no loss balancing), and (c) $\gamma^2 \approx 0.998$ with loss balancing ($\delta = 0.012$). The source is a 10 Gb/s $2^{11}-1$ PRBS pattern with $\phi_d = 0.01\frac{\pi}{2}$, $\phi_{bias} = 0.52\pi$, $\phi_m = 0.48\pi$.

average ON state power to the average OFF state power. Since the OFF state power can vary significantly when the losses are dithered and $\gamma^2 \approx 1$, we instead consider the worst case extinction ratio, ER_{worst}, which is also the eye opening. For the eye diagrams in Figure 3.8 having $\gamma^2 \approx 0.7$, $\gamma^2 \approx 0.85$, and $\gamma^2 \approx 0.998$ the eye openings are approximately 20.7 dB, 27.0 dB, and 41.3 dB respectively. This can be expressed semi-analytically as the minimum ON state power divided by the maximum OFF state power,

$$ER_{worst} \approx \frac{1 + \gamma_{tuned}^2 e^{-\delta} + 2\gamma_{tuned} e^{-\delta/2} \cos\left(\phi_{bias} - \phi_m + \phi_d\right)}{1 + \gamma_{tuned}^2 e^{-\delta} + 2\gamma_{tuned} e^{-\delta/2} \cos\left(\phi_{bias} + \phi_m - \phi_d\right)}. \tag{3.18}$$

The worst case extinction ratio can be further reduced based on the input signal randomness since the source driver and MZM electrodes typically have lowpass frequency responses which have memory [53]. With source encoding (e.g. 8b/10b encoding), this randomness can be reduced and eye openings predicted by equation 3.18 are possible.

3.4 Extension to Multiple Nested MZIs

If an MZM with nested MZIs is used, such as the DPMZM in Figure 2.3, the complex phase biasing method outlined in this chapter can be extended in a straightforward way. Each nested MZI can be biased using the same method as an individual MZI with their own dithering signals and feedback control. Additionally, using nested MZIs can reduce the output amplitude variation due to dithering tones by applying the dithering tones to pairs of nested MZIs which are out of phase. Specifically, the real phase dither tones in the top MZI and bottom MZI should have the same amplitude and frequency, and their relative electrical phase will depend on the operating point and modulation format as discussed in [54–56] where this has been demonstrated. Similarly, the output loss variation due to dithering the imaginary part of the phase (Equation 3.17) can be reduced by applying equal amplitude and frequency loss dithering signals to pairs of nested MZIs which are π out of (electrical) phase.

3.5 Summary

An any-point complex phase biasing and locking method for MZIs was developed using low frequency, small amplitude dither tones to perturb the system. Using a realistic system model of an MZM implemented in MATLAB, this method of complex phase biasing can dynamically measure the complex phase of an MZM device to an accuracy of less than 1% and can be used to maintain an operating point in the presence of ambient phase drift. A typical MZM with $ER_M \lesssim 20$ dB could be tuned to have maximum extinction ratios in excess of 40 dB using this method with practical operating parameters. Dithering the losses causes the insertion loss to vary proportionally which can be compensated using an optical amplifier and can also be mitigated if multiple nested MZIs are used. One tradeoff of using this method is that it limits the dynamic extinction ratio of a given MZI which cannot be compensated during dynamic operation. Nonetheless, the complex phase biasing method will generally improve the extinction ratio up to that limit.

Chapter 4

Practical Considerations in SOI and Future Work

An SOI photonic integrated circuit (PIC) consisting of MZMs with built-in complex phase shifting elements and output PDs was fabricated at the A*STAR Institute for Microelectronics (IME) to test the complex phase biasing method discussed thus far. In this chapter, measured data from fabricated complex phase biasing elements are presented and their practical issues are discussed. The shortcomings of the current design and methods of improvement are discussed. We focus on the relative changes in the real and imaginary parts of the phase of the fabricated devices which are necessary for complex phase biasing. The chapter concludes with a discussion of future work.

4.1 Fabricated Photonic Integrated Circuit

The PIC was fabricated in the IME baseline silicon photonics process [17, 57, 58] and consists of calibration test structures of individual phase shifting devices and two MZM structures which are identical except for their high-frequency electrode geometry. Each MZM has 2×2 adiabatic 50/50 couplers at the input (only one input port excited) and output for broadband even splitting [36]. The complementary port of the output is connected to an on-chip PD from the IME design kit [57, 58], which is meant to provide a signal for the feedback control loop. The purpose of connecting

the PD to a complementary port at the MZM output rather than tapping-off some of the output optical signal was to obtain more output power at both ports. Using this method is problematic if the output coupler splitting ratio is not exactly 50/50 since the loss biasing will only apply to the complementary port (see Appendix A). One method of alleviating this issue is to characterize the output coupler at startup and factor in the difference into the analysis, but this assumes that the output splitting ratio will be constant during dynamic operation (depending on design, it may change due to heating for example). For this reason, a more robust design would combine both the signals at the output and tap off a percentage of the output power to the feedback control system as was shown in the previous chapter. Using a tap-off coupler will incur a loss penalty at the output which depends on the tap-off coupler splitting ratio.

The phase shifters to bias the real and imaginary parts of the MZM phase difference are made with resistive heaters and forward biased PIN diodes integrated into the waveguides in both arms of the MZMs. High-frequency phase shifters for modulation in each arm of the MZMs are comprised of PN diodes across the waveguide cross section connected to transmission lines that form travelling-wave electrodes (TWEs) with one MZM using a coplanar waveguide (CPW) geometry and the other using coplanar strips (CPS). The principle of operation, device geometry, measured data (where available), and a discussion of the practical issues and methods of improvement for each of these devices is presented in the following subsections. A schematic of an MZM on the fabricated PIC with CPS transmission lines is given in Figure 4.1.

Channel waveguides with a cross section of $width \times height = 500$ nm $\times$ 220 nm [58] (refer to Figure 1.2) are used to connect the MZMs and calibration structures. This waveguide geometry provides better confinement for the transverse electric (TE) polarization than transverse magnetic (TM) and thus TE is preferable to use for dense integration. Specifically, the effective indices for each polarization are about $n_{eff,\mathrm{TE}} = 2.5$ and $n_{eff,\mathrm{TM}} = 1.85$ at $\lambda = 1.55$ μm.

The optical input to the chip consists of a tunable wavelength laser through a

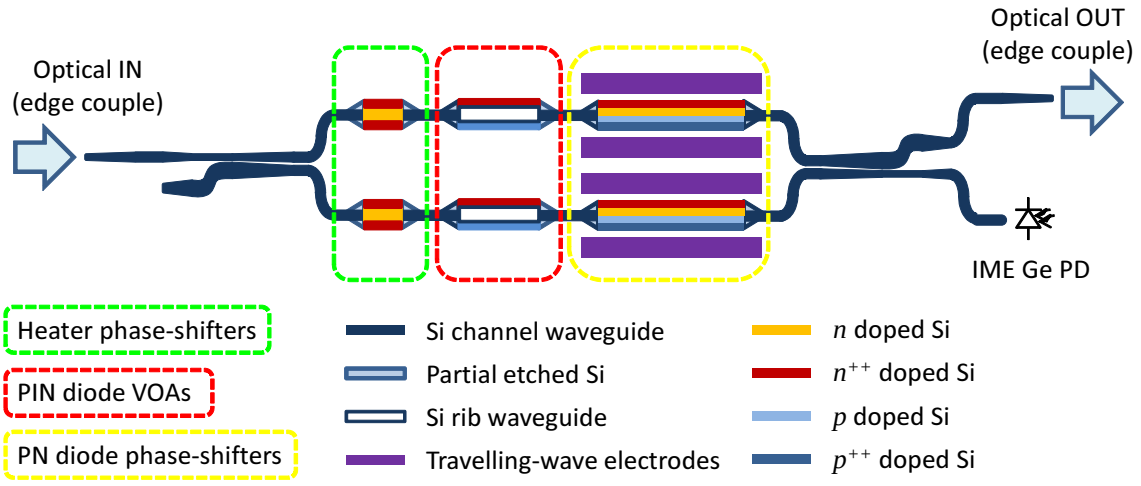

Figure 4.1: Schematic of fabricated MZM (not to scale) with integrated heaters, PIN diodes, CPS TWE PN diodes, and an output PD. Electrical contact pads and wiring not shown.

single mode fiber (SMF) and polarization rotator to a lensed fiber ($1/e^2$ diameter = 2.5 μm at $\lambda = 1.55$ μm) to obtain a better mode overlap with the highly confined on-chip silicon waveguides. To reduce the coupling losses between the lensed fiber and the on-chip waveguides, the input and output edge couplers were formed with a small core ($width = 200$ nm) waveguide which has a de-localized TE mode and provides better overlap with the lensed fiber mode. The waveguide coupler was then adiabatically widened over a length of 200 μm to the standard core width of 500 nm to adjust the spot-size for better waveguide confinement. Finite-difference time-domain (FDTD) simulations performed on these couplers gave a flat spectrum over $\lambda \in [1.5, 1.6]$ μm with theoretical coupling and spot-size conversion losses lower than 1 dB for both TE and TM. The measured devices had loss of about 2 dB per coupler, consistent with typical inverse edge couplers. The optical output of the MZM went through a lensed SMF into an off-chip PD.

To ensure the light is TE polarized, a waveguide with many 5 μm radius bends to radiate TM light is tested. To set the polarization to TE, continuous wave light is passed through this structure and the polarization is adjusted until the highest transmission is obtained through the device. During electrical measurements, both the current through and voltage across test devices are measured.

4.1.1 Heater Phase-shifters

Using the strong thermo-optic effect in silicon, the effective index, and thus the real part of the phase of a waveguide can be adjusted by changing the temperature since $\phi_r = \frac{2\pi n_{eff}}{\lambda} L$, where L is the waveguide length. Resistive heaters were formed to bias the real part of the optical phase by doping silicon waveguides as shown in Figure 4.2a. For all devices discussed, there is upper and lower SiO_2 cladding and electrical contact is made from metal pads above the devices to the highly doped (n^{++} or p^{++}) regions using vertical interconnect access (VIAs).

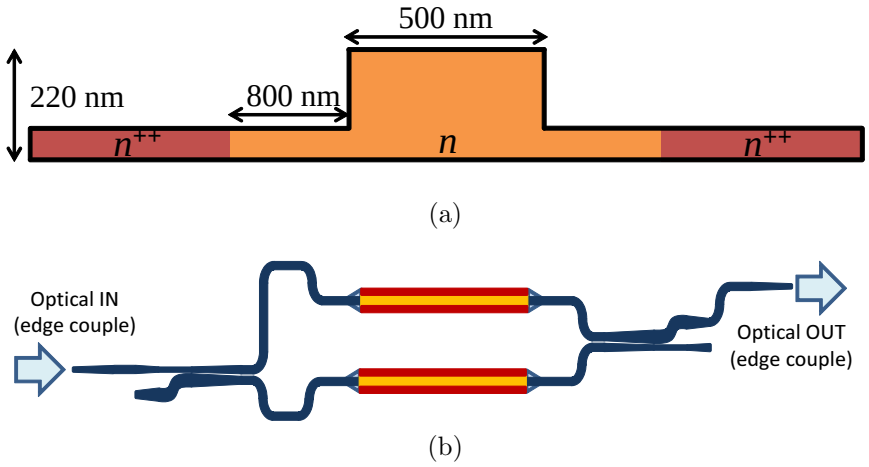

Figure 4.2: (a) Cross section of a resistive heater phase shifter formed by doping a silicon waveguide and (b) Unbalanced MZI with heaters in each arm (not to scale). Doping concentrations and etch depth are IME process parameters [58].

Originally, these heaters were designed to ensure a phase shift greater than 2π was possible with a small applied voltage. Consequently, the heaters, which were 250 μm long were much longer than necessary for dithering. To determine the change in the loss and real part of the phase in the heaters as a function of voltage (current), two calibration structures were tested. The first calibration structure was simply a heater connected to input and output waveguides at either end. Using this structure, the applied loss can be determined by monitoring the output transmission while varying an applied voltage (current). The second calibration structure consisted of a length imbalanced MZI (to provide a finite free spectral range) with a heater in each arm as shown in Figure 4.2b. The real part of the phase shift can be obtained by monitoring

how the optical transmission spectrum shifts as a voltage is applied to one of the heaters. Specifically, the change in the real phase difference between MZI arms is

$$\Delta\phi_r \approx 2\pi \frac{\Delta\lambda_d}{\Delta\lambda_{FSR}}, \tag{4.1}$$

where $\Delta\lambda_d$ is the wavelength shift of any transmission spectral feature (for simplicity, we monitor the "dip wavelength" where the transmission is minimum) and $\Delta\lambda_{FSR}$ is the wavelength free spectral range (FSR) of the transmission spectrum. The heater was tested with constant current increments to ensure large currents ($\gtrsim$ 50 mA) which could damage the wires connecting devices would not be applied. Spectral measurements for several different applied currents to the heater MZI are shown in Figure 4.3.

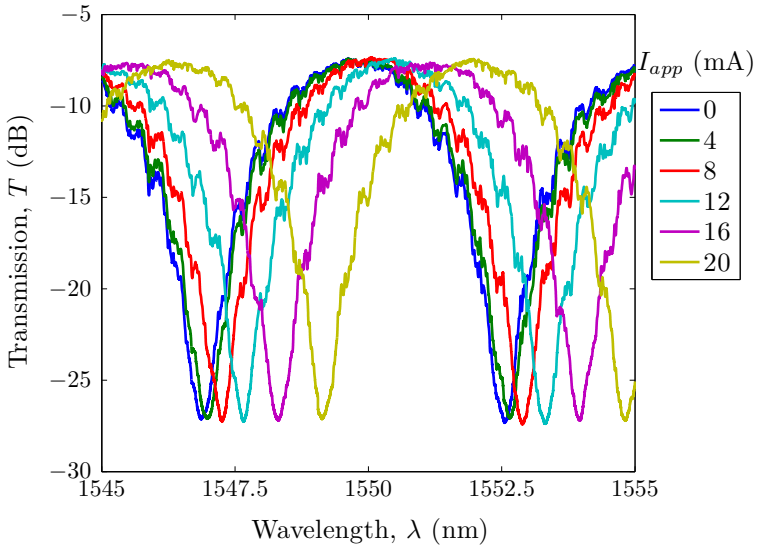

Figure 4.3: Heater MZI optical transmission spectrum for several DC input currents.

The heater MZI uses the same adiabatic couplers as the fabricated MZM designs and from Figure 4.3 the maximum extinction ratio is $\sim$ 20 dB, indicating $\gamma^2 \approx 0.669$. The maximum transmission is -7.4 dB which is mostly due to excess waveguide length and the edge couplers ($\sim$2 dB each). By reducing this length and neglecting one of the edge couplers, on-chip losses of about 5 dB are possible, justifying the excess loss model choice in Chapter 3.

The length normalized change in the real part of the phase ($\Delta\beta$ in some texts [59])

and the loss of the heater as a function of voltage are given in Figure 4.4.

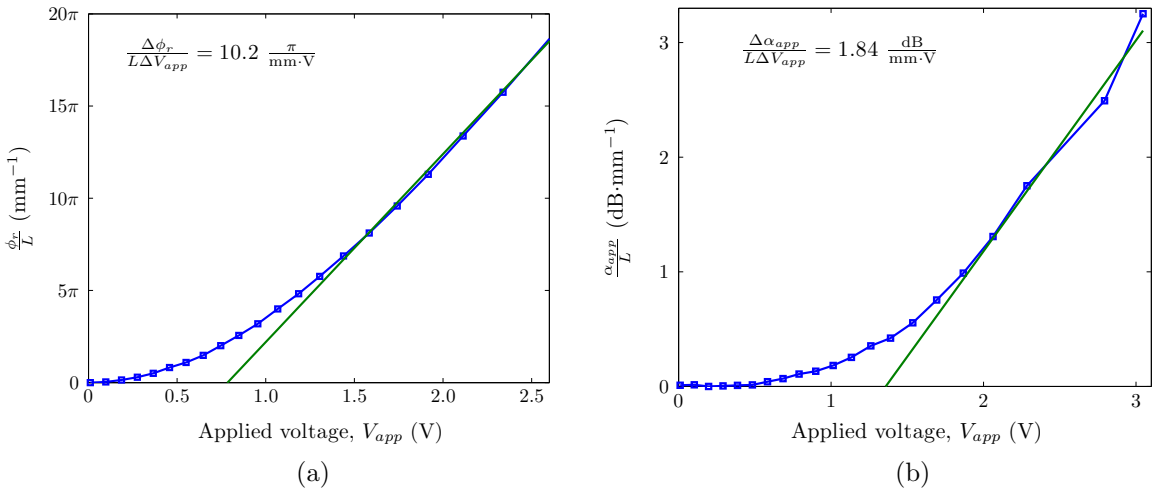

Figure 4.4: Heater transfer functions for the change in the length normalized (a) real component of phase and (b) attenuation as a function of voltage.

The heaters will be used to bias the real component of the phase difference in the MZM, but they have a parasitic loss shift which was not considered in the analysis of Chapter 3. The parasitic loss change in the heater is about 1% of the magnitude of an applied shift in the real component of the phase which adds a small loss dithering tone at f_d. This changes the expressions for the spectral amplitudes at the harmonics of the phase dithering frequency by several small factors which depend on ϕ_{bias} and ϕ_d. Fortunately since the changes are small, the simple relations derived in the previous chapter are still approximately true. To see the effect the parasitic loss dither has on calculating the complex phase bias, the system model from Chapter 3 was re-simulated at complex phase biases across the range $\gamma^2 = [0.6, 0.7, 0.8, 0.9, 0.95, 0.998]$ and ϕ_{bias} from $-\frac{3\pi}{4}$ to π in increments of $\frac{\pi}{4}$ as shown in Figure 4.5. It was found that for $\phi_d = 0.01\frac{\pi}{2}$ to $0.05\frac{\pi}{2}$, the effect of the heater parasitic loss dither caused a maximum error in calculating γ^2 and ϕ_{bias} of $< 2\%$ each.

In Chapter 3, the components modelled to bias the real part of the MZM phase difference were assumed to have a linear transfer function with respect to voltage which is not true for heater phase shifters. The real phase dither signal must operate in a linear region of the transfer function so that ϕ_d is known and the spectral amplitudes at the harmonics of the dither signal are not distorted which would increase the

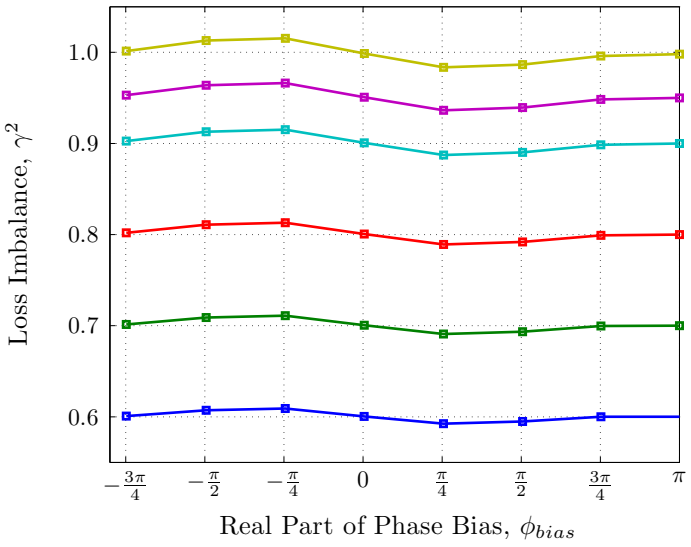

Figure 4.5: Calculated values of complex phase bias considering parasitic loss dither from heater phase shifter with $\phi_d = 0.01\frac{\pi}{2}$ and $\delta = 0.012$ over the range of $\gamma^2 = [0.6, 0.7, 0.8, 0.9, 0.95, 0.998]$ and $\phi_{bias} \in [-\frac{3\pi}{4}, \pi]$ in increments of $\frac{\pi}{4}$. The worst case errors for calculated values were $< 2\%$ for both ϕ_{bias} and γ^2.

error in determining ϕ_{bias} and γ^2. From Figure 4.4a, the phase transfer function of the heater is approximately linear with a slope of $10.2 \times \pi$ $(\text{mm} \cdot \text{V})^{-1}$ for applied voltages ≥ 1.5 V, so it is desirable to bias the dither signal in this operating range.

The sensitivity of the phase change with respect to voltage must also be considered to achieve a small ϕ_d. The fabricated heater is 250 μm long and thus has a sensitivity of $\sim 2.55 \times \pi$ V^{-1} when operating in the linear region of the transfer function. The voltage amplitude required to achieve $\phi_d \sim 0.01\frac{\pi}{2}$ is about 2 mV which may be difficult to reliably generate from a D/A. Since the DC component of the real part of the phase bias does not need to have a linear transfer function or require high sensitivity, a better design could instead use two separate heaters for the DC and dither components of the real part of the phase bias signal. This way a higher resistance heater can be designed for the sensitive phase dithering signal and a lower resistance heater can be used to bias the phase with low voltages. There are several methods to producing a higher resistance heater such as reducing the length, increasing the distance between the waveguide core and highly doped contact regions, or even changing the dopant type. Using p type doping in the same process will increase the heater resistance and thus sensitivity by almost a factor of 2. As an example, if we assume the minimum

swing that can be reliably generated is 50 mV, we could design a sensitive heater for the dither signal using the geometry of Figure 4.2a, which is 10 μm long, and bias it at $\sim$ 1.5 V so that a phase dither swing, $\phi_d \approx 0.01\frac{\pi}{2}$ can be attained with a 50 mV voltage swing. A longer heater such as the one which was fabricated could then be placed after the sensitive heater for the DC biasing. This is shown schematically in Figure 4.6:

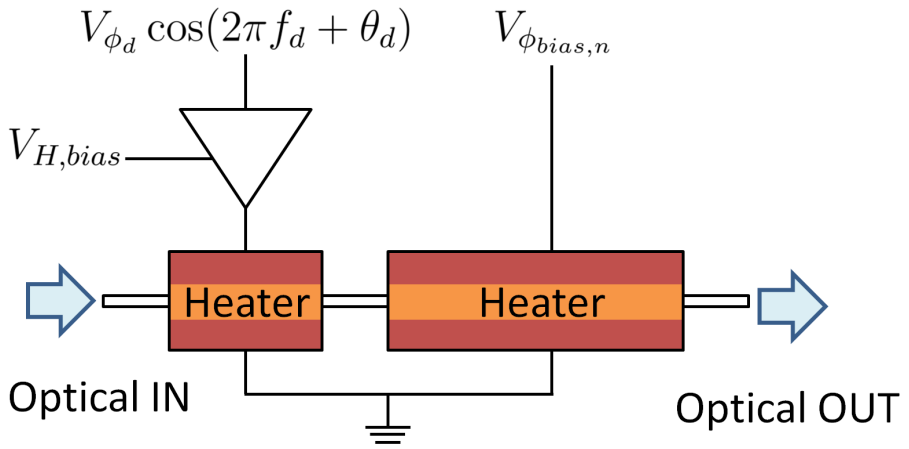

Figure 4.6: Schematic of a circuit to change the real part of a waveguide phase consisting of a sensitive heater biased to operate with a linear transfer function and a less sensitive heater to change the DC phase with a small voltage.

where $V_{H,bias}$ is the sensitive heater bias which ensures the heater is operating in a linear region of the transfer function ($V_{H,bias} = 1.5$ V for this design), V_{ϕ_d} is the voltage amplitude to dither the real component of the phase bias, and $V_{\phi_{bias,n}}$ is the applied DC voltage to shift the real part of the phase bias in the n^{th} waveguide. The buffer which is used for biasing the sensitive heater in the figure can be made from a variety of operational amplifier circuits for example, and could include gain or attenuation if desired. If a unity gain biasing buffer is used, the amplitude of the phase dither can be written as $\phi_d \approx (0.1 \times \pi\ \text{V}^{-1})\, V_{\phi_d}$ and the DC shift in the real part of the phase bias is the sum of the phase shifts caused by $V_{H,bias}$ and $V_{\phi_{bias}}$, $\phi_{bias,n} = f(V_{H,bias}) + f(V_{\phi_{bias}})$, where the f indicates the transfer function for each heater.

4.1.2 PIN Diode Variable Optical Attenuators

PIN diodes integrated across waveguides were designed for use as VOAs with a structure shown in Figure 4.7. The device is operated in forward bias (positive voltage applied to the p^{++} region with respect to the n^{++} region) which causes carrier injection into the waveguide core. In forward bias, the plasma dispersion effect yields a reduction in the waveguide effective index and increase in loss [14]. The fabricated PIN diode waveguides were 500 μm long.

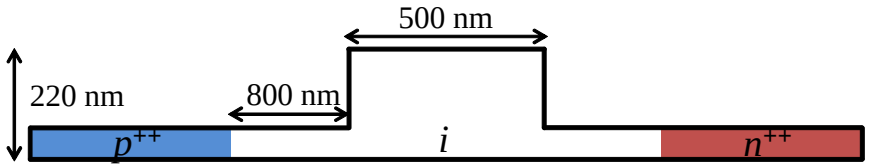

Figure 4.7: Cross section of a PIN diode VOA and phase shifter formed by doping a silicon waveguide. Doping concentrations and etch depth are IME process parameters [58].

The PIN diodes were characterized in the same way as the heaters, with one calibration structure for determining loss shift as a function of voltage and another length imbalanced MZI structure to determine the real part of the phase shift as a function of voltage. The length normalized change in the real component of the phase and the attenuation as a function of voltage for the PIN structure are shown in Figure 4.8 starting at the turn-on voltage of ~ 0.8 V.

The transfer functions of the change in the real part of the phase and the loss of the PIN diode as a function of voltage are fairly linear for applied voltages between 1 and 1.4 V. Since we intend to use this device as a VOA, it would be preferable to eliminate the parasitic change in the real part of the phase with respect to voltage. Unlike the parasitic effects in the heater phase-shifter, the parasitic phase shift in the VOA is very large and cannot be neglected. For a given loss change, there is change in the real part of the phase which is almost 5$\times$ greater. Since the direction which the real part of the phase changes in a PIN diode is opposite to the heater in the previous section, we can use a heater to offset the parasitic change in the real part of the phase. A nearly ideal VOA can be formed by connecting a heater and

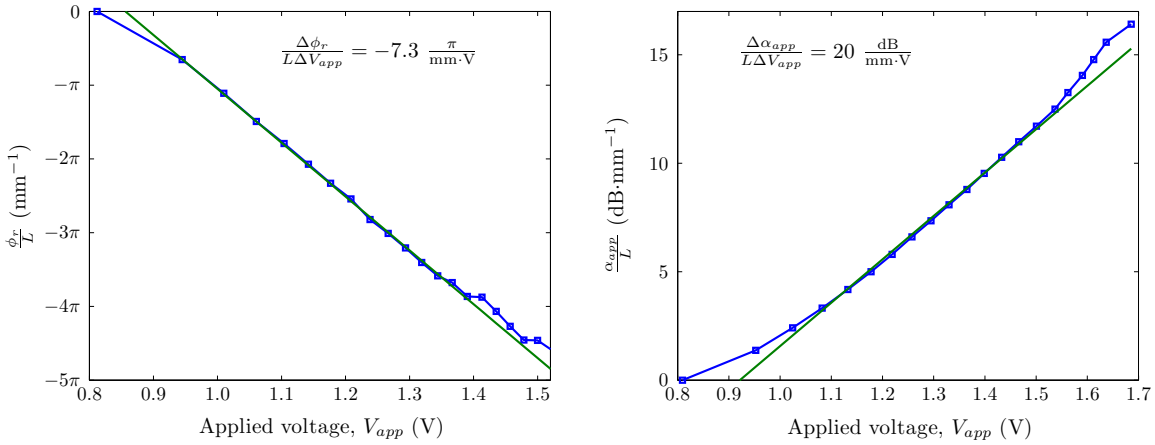

Figure 4.8: PIN diode transfer functions for the change in the length normalized (a) real component of phase and (b) attenuation as a function of voltage.

PIN diode with a common applied voltage and independent bias voltages as shown in Figure 4.9, where $V_{H,bias}$ is the heater bias voltage, $V_{PIN,bias}$ is the PIN diode bias voltage, and V_{VOA} is the common applied voltage to both the heater and PIN diode forming the VOA. The bias voltages $V_{H,bias}$ and $V_{PIN,bias}$ are chosen such that the heater and PIN diode are both operating in linear regions of their transfer functions. The lengths of the heater and PIN diode and/or the gain of their buffer stages need to be appropriately chosen to cancel out the real component of the phase change. If the parasitic phase change in the VOA can not be completely cancelled, the ability to calculate the complex phase bias will be degraded similar to what was shown for the heater. Fortunately, even with the parasitic loss dither from the heaters and assuming the VOAs have a parasitic change in the real part of the phase of up to 5% the magnitude of δ, the error in calculating the complex phase bias is still less than 2%. The feedback control simulation with drifting phase from Chapter 3 was performed considering these parasitics and still yielded an eye opening of 40.2 dB.

The VOA shown in Figure 4.9 can be implemented using the fabricated chip since each arm of the MZMs has a heater and PIN diode as shown in Figure 4.1. The fabricated chip can have linear VOAs by setting $V_{H,bias} = 1.5$ V and $V_{PIN,bias} = 1$ V and the gain of the heater buffer to be 80% of the PIN diode buffer. The sensitivity of a VOA implemented with the fabricated circuit will be about 10.37 dB $\cdot$ V^{-1} for a

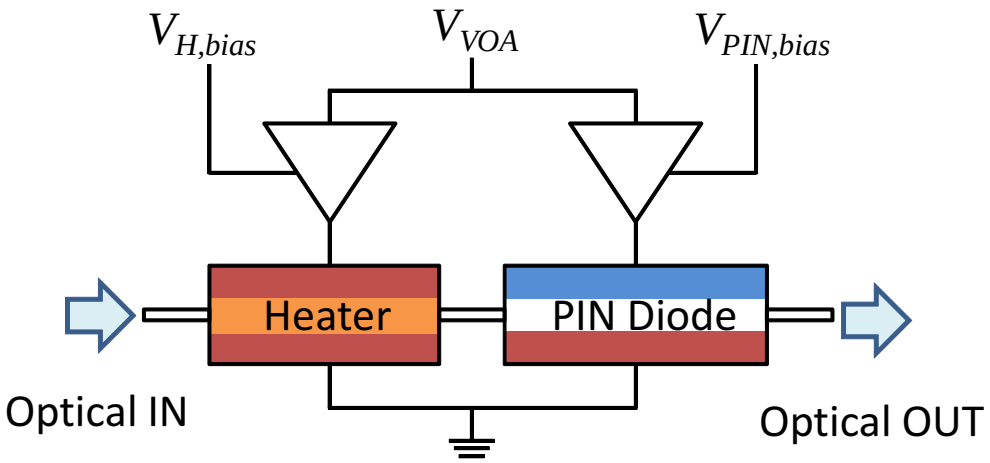

Figure 4.9: Circuit schematic of a VOA consisting of a heater and PIN diode of differing lengths which are independently biased.

unity gain PIN biasing buffer due to the long heater and PIN diode lengths. If we again assume we can get a minimum reliable voltage swing of 50 mV, that implies a value of $\delta \approx 0.12$ which is an order of magnitude greater than the value that was simulated to have low penalties. An improved design for loss biasing would be similar to the heater phase biasing design in which one VOA would be designed for high sensitivity operation for the loss dithering, and another lower sensitivity VOA would be designed for DC loss biasing. To obtain $\delta \approx 0.012$ with a 50 mV voltage swing, the same design could be used with a heater and PIN diode length scaled by a factor of 10 (heater length = 25 μm and PIN length = 50 μm). Smaller values of δ are also possible by further device scaling.

4.1.3 Travelling-wave Electrode PN Diode Phase-shifters

The emphasis of this work is on complex phase biasing rather than RF design, so this section will focus on the effects that the high frequency phase shifters have on the ability to bias the complex phase and some system performance considerations rather than design considerations for the RF components which are widely studied [53].

The fastest known method to efficiently modulate the real part of the phase of a silicon waveguide is by the plasma dispersion effect in depletion operation. For this reason, most high-frequency optical modulators in silicon including those in this

design, employ a reverse biased PN junction integrated into a waveguide to modulate the diode depletion region width using a reverse biased source [15, 17, 57, 60–63]. The PN diode bias can be slightly forward biased while still operating in depletion before significant recombination of carriers takes place near the turn-on voltage [60]. A cross section of the PN diode integrated into a waveguide in this design, based on the designs in [57, 60], is shown in Figure 4.10.

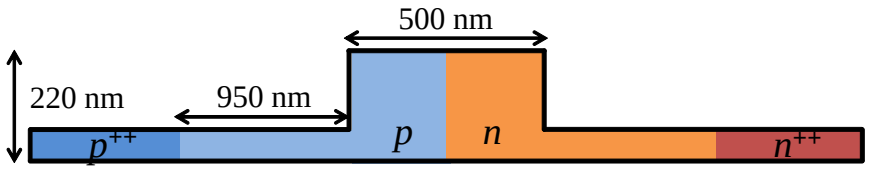

(a)

Figure 4.10: Cross section of the PN diode phase shifter formed by doping a silicon waveguide with geometry based on the designs in [57, 60]. Doping concentrations and etch depth are IME process parameters [58].

When the PN diodes are operated in reverse bias, the depletion region is widened which lowers the overlap of the optical mode with charge carriers. This lowers the optical loss and increases the real part of the phase [14]. The change in the real and imaginary parts of the phase are nonlinear with voltage and depend on the doping profile and waveguide geometry [64]. At the time of writing this, measured data from the fabricated PN diode phase shifters have not been taken. A PN diode phase shifter which was fabricated in the same process technology with a very similar geometry to this design is demonstrated in [60]. The PN diode phase shifter length in [60] was 5 mm long while our fabricated design was 4 mm long. The real part of the optical phase change as a function of an applied reverse biased voltage for the PN phase shifter in each arm of an MZM in [60] is given in Figure 4.11.

From Figure 4.11, the DC switching voltage required to incur a phase shift of π is $V_{\pi,DC} \gtrsim 5.5$ V for each arm of the MZM. Since the device fabricated for this work was shorter than the device in [60] by 20%, we could expect the DC switching voltage to be about 25% larger, on the order of 7 V. The nonlinear electro-optic response of the PN diode contributes to optical pulse shaping. The PN phase shifters in [60] have

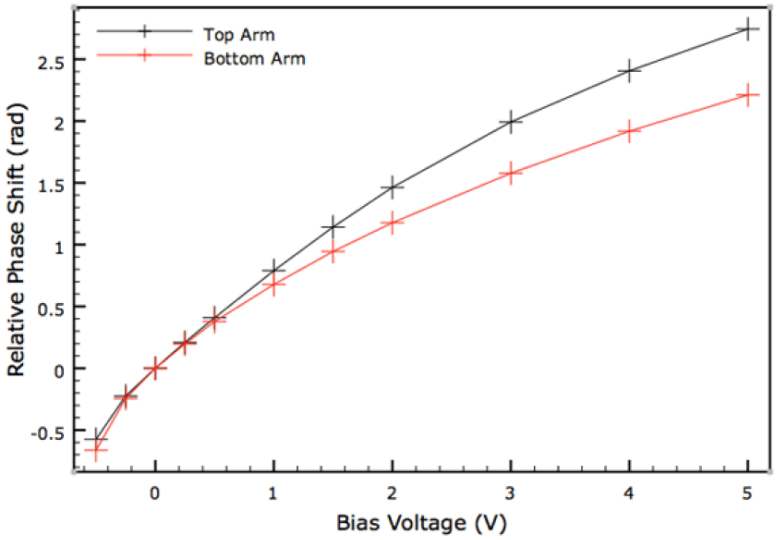

(a)

Figure 4.11: Change in the real component of optical phase for 5 mm long PN diodes in the arms of an MZM as a function of an applied reverse biased voltage (taken from [60]). The diodes were designed to be identical but their transfer functions differ due to fabrication imperfections.

slightly different transfer functions for the top and bottom arms of the MZM which makes the push-pull response of the MZM and associated chirp difficult to predict. There are methods of mitigating this effect based on the circuit mask layout which were considered in this design so that the transfer functions of the phase change with respect to voltage in each arm of the MZMs should be nearly identical.

The PN diode waveguide optical loss as a function of applied voltage was not characterized in [60] but simulation results show that the change in loss is around an order of magnitude smaller than the change in the real part of the phase which can not be neglected [65]. The analysis in Chapter 3 assumed that the waveguide losses were constant other than the loss dithering signal, but the PN junction phase shifters actually modulate the losses with a high-frequency signal proportional to $\phi_s(t)$. This means that the modulator will have state-dependent losses which will depend on the modulation format and driving signals. The analysis to find the average γ using Equation 3.11 is still valid, but the target value for optimal performance will no longer be $\gamma_{tuned} = 1$. In Chapter 2, the phase error due to MZM arm loss imbalance was shown to be most prominent when the normalized transmission through the MZM

was $\lesssim 0.5$ (see Figure 2.5). Additionally, for maximum extinction ratio, the MZM arm losses must be balanced when the MZM normalized transmission is minimum. For these reasons, the optimal operating point will be set if $\gamma = 1$ when the MZM transmission is minimum. This can be achieved by setting the average loss imbalance, γ_{tuned} to be the inverse of the loss imbalance when the MZM transmission is minimum, γ_{OFF}. The loss imbalance at minimum transmission, γ_{OFF}, depends on the bias point and modulation format but can be approximately determined from a static measurement of the losses with respect to voltage of the MZM arms. A method to determine γ_{OFF} dynamically is a topic of future work.

In silicon MZMs, the high-frequency phase shifters are typically multiple millimetres long which make the electrodes and diodes very capacitive which reduces bandwidth if treated as lumped elements. To increase bandwidth, distributed electrodes are designed using transmission lines with a microwave group index matching the optical group index of the mode being modulated [53]. For TE polarization in the silicon waveguide geometry being used at $\lambda = 1.55$ μm, the optical group index is $n_g \approx 3.86$. In the fabricated circuit, two types of transmission line geometries, CPW and CPS based on the designs in [57] and [60] respectively, were implemented on two different MZMs to try to match the microwave and optical group indices. The geometry of CPW and CPS TWEs are shown in Figure 4.12, where 'G' indicates a ground connection and 'S' indicates a (positive) signal connection for reverse bias operation.

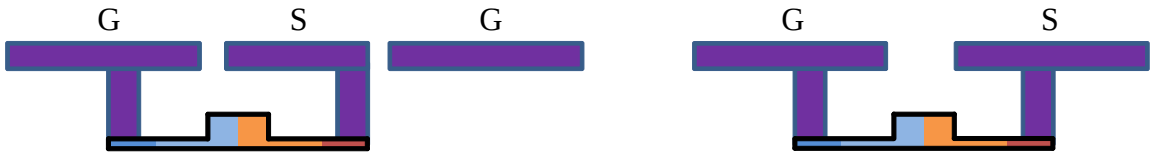

(a) (b)

Figure 4.12: Cross section of an integrated travelling-wave electrode PN diode phase shifter in reverse bias using (a) coplanar waveguide transmission line geometry and (b) coplanar strips. Purple blocks indicate RF lines and VIAs.

The microwave characteristic impedance (Z_m) and propagation constant (γ_m, which contains the microwave effective index) of the TWEs can be computed with high

accuracy using closed-form analytic solutions based on the TWE geometry [66, 67]. The TWEs were designed to have a characteristic impedance close to 50 Ω to match the impedance of our cables and drivers for testing, and a group index close to 3.86 at 10 GHz (nominal frequency). To prevent reflections, the TWEs must be terminated in matched impedances as shown in Figure 1.3. The high-frequency phase shifters have a low-pass electro-optic transmission (S_{21}) due to the RF losses in the conductors. This low-pass response contributes to pulse shaping and can reduce the maximum phase swing, ϕ_m, if the modulation frequency is increased and a constant phase bias and voltage swing are maintained [53]. This effect can degrade the ER and/or maximum transmission, but a high ER can still be obtained by shifting the real part of the phase bias which will incur additional insertion loss (Equation 2.11).

4.2 Future Work

4.2.1 Experimental Demonstration of Automated Complex Phase Bias Locking

The next step in this work is to demonstrate the proposed method of complex phase measurement and bias locking in a physical system. For the first experimental demonstration, the fabricated PIC can be used with a summation of input signals into the heaters and PIN diodes for the dithering and bias signals. A tap-off coupler for a feedback signal proportional to the MZM output can be formed using a fiber directional coupler at the optical MZM output to an off-chip PD. In the first experiments, the dither tones can be generated, monitored, and manipulated with lab equipment (e.g. signal generator and D/A to computer) rather than a compact circuit. As mentioned in the previous sections, the sensitivity of the heaters and PIN diodes on the fabricated PIC may not be low enough to perform small signal dithering due to the finite D/A resolution on signal sources which could cause performance penalties. In addition, Fabry-Perot resonances in the circuit (e.g. due to the air gap between lensed fiber and edge coupler, and edge coupler to edge coupler with air on either end) may

reduce the observable extinction ratio. This effect can be mitigated by using an index matching fluid between the input and output fibers and edge couplers.

Once the basic concept of complex phase measurement has been demonstrated in a physical system, there are several avenues of research that can be pursued. Since this is the first proposed method to enable real-time measurement of an MZI loss imbalance during dynamic operation, the effects of complex phase bias drift over time in the presence of environmental changes (e.g. temperature) on modulator performance can be studied. Using complex phase bias locking to improve the extinction ratio, phase error, and the ability to calculate MZM chirp should also be experimentally verified. The effects of state-dependent MZM arm loss imbalance from the high-frequency phase shifters mentioned in the previous section should be studied more thoroughly to determine if there is a method to dynamically measure the MZM arm loss imbalance in the OFF state (γ_{OFF}) for more robust performance. The improvements and penalties of applying complex phase biasing and locking to other MZI devices including high ER filters, multi-port switches, and analog modulators could also be investigated more thoroughly. The concept of real-time complex phase locking can also be investigated in applications which use other modulator and filter technologies including resonant devices.

4.2.2 Resonant Devices: Microrings

A microring resonator is an attractive structure to implement compact filters and low energy per bit modulators on SOI [68–71]. The quasi-static transmission of the through-port of a microring resonator is given by

$$T_r = \frac{a_r^2 + |t_r|^2 - 2a_r|t_r|\cos\phi_r}{1 + a_r^2|t_r|^2 - 2a_r|t_r|\cos\phi_r}, \tag{4.2}$$

where a_r is the loss coefficient in the ring which includes the coupler loss and the round-trip loss through the ring (equivalent to a_n in an MZI arm), t_r is the through-port coupling coefficient, and ϕ_r is the round-trip optical phase change (real part) in the ring including the through-port coupling phase [72]. The through-port extinction

ratio of a ring resonator depends on a loss balance much like an MZI. The maximum extinction ratio of a ring resonator is determined by dividing the maximum transmission (at anti-resonance) by the minimum transmission (at resonance). If we define a field loss imbalance term for the ring as $\gamma_r = \frac{a_r}{|t_r|}$, the maximum extinction ratio is

$$ER_{M,r} = \left(\frac{1+\gamma_r}{1-\gamma_r}\right)^2 \left(\frac{1-a_r|t_r|}{1+a_r|t_r|}\right)^2. \tag{4.3}$$

The first term of Equation 4.3 is very similar to the maximum extinction ratio for an MZI (Equation 2.3). The condition where $\gamma_r \to 1$ is called critical coupling which provides the greatest $ER_{M,r}$ which can be desirable to achieve for use in high rejection filters or high ER modulators for example. If critical coupling is desired, the loss coefficient and through-port transmission coefficient must be known in the device design which will both vary due to fabrication uncertainties such as waveguide roughness and dimensional variation [73]. To overcome these uncertainties in a similar method to statically biasing the losses in an MZI, ring resonators operating in the under-coupled region ($\gamma_r < 1$ before tuning) with an optical amplifier integrated into each ring have been demonstrated to statically tune the gain to achieve critical coupling [74–76]. In a similar manner, we designed a microring modulator on our fabricated PIC with an integrated VOA which is very over-coupled ($\gamma_r > 1$) prior to tuning. In this way, the ring losses can be adjusted to achieve critical coupling and increase the linewidth which can be desirable for high extinction, high bandwidth modulators. A schematic of the fabricated ring modulator with a PIN diode for loss tuning and a simulated transmission spectrum for $t_r = 0.97$ which shows an increase $ER_{M,r}$ after loss tuning (neglecting the real part of the phase shift) are shown in Figure 4.13. The study of real-time loss measurement, control, and performance effects in microring modulators similar to that proposed for MZMs in this thesis is a subject of future work.

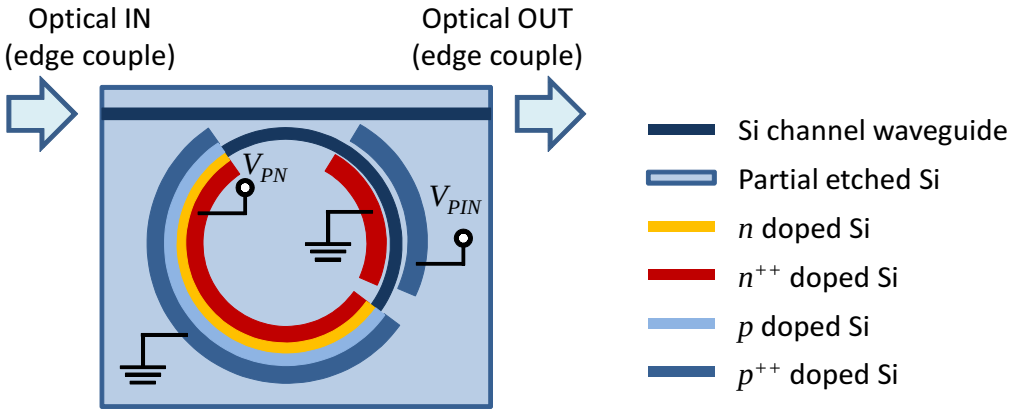

(a)

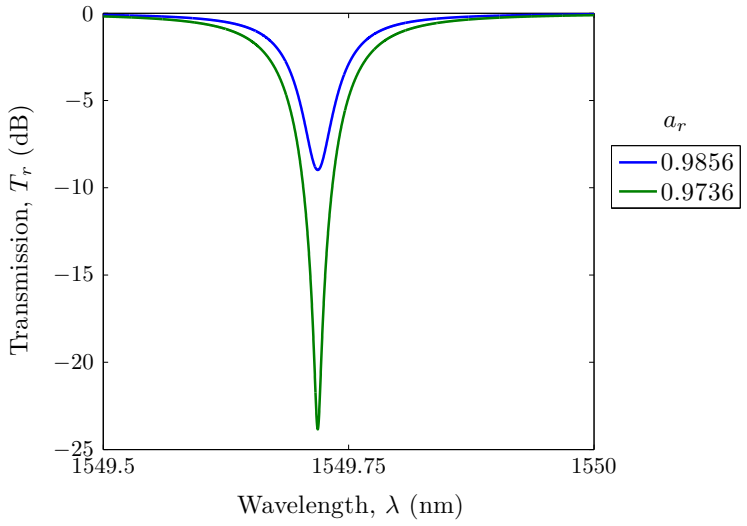

(b)

Figure 4.13: (a) Ring modulator with PN and PIN phase shifters for modulation and loss tuning and (b) transmission spectrum without and with loss balancing (neglecting real part of the phase shift from PIN diode). The spectrum calculation uses a ring with a 20 μm radius, the same phase shifter geometry for the MZM in this chapter, 10 dB/cm intrinsic loss due to doping (based on [60]), and through port coupling of $t_r = 0.97$.

Chapter 5

Conclusions

5.1 Summary of Results

This thesis presented the first proposed method to determine and adjust the complex phase bias of an MZI device to any operating point during dynamic operation. We extended the most common approach of biasing the real part of an MZM phase bias to complex phase. The method proposed in this work can be used to set and maintain the complex phase bias of an MZM to an operating point which effectively eliminates the phase error at the output (within the tolerance of the measurement and tuning capabilities), allows a more accurate characterization of the modulator chirp, and improves the extinction ratio.

In Chapter 2, we introduced the inherent loss imbalance between arms in an MZM due to fabrication imperfections and investigated the resulting effects on modulator performance. We showed that the arm loss imbalance in an MZM leads to a degraded extinction ratio, adds phase error at the output, and makes the modulator chirp difficult to determine. We showed that statically tuning the losses in each arm of the MZM can improve the extinction ratio, reduce the output phase error, and allow a more accurate calculation of the chirp. By statically tuning the losses, we showed that there is a penalty on the insertion loss and optical modulation amplitude which are typically both $\lesssim 1$ dB and can both be addressed using optical amplification after

the transmitter stage in a communication link.

In Chapter 3, we examined the most prominent method of setting and locking the real part of an MZM phase bias and then proposed an extension of that method for complex phase biasing using variable optical attenuators (VOAs) integrated into the MZM arms. We first explained how the real part of an MZM phase is determined by applying a low frequency, low amplitude dither tone to the real part of the phase and monitoring and manipulating the spectral content at the MZM output. We then proposed a new method to set the complex phase bias based on a similar dithering technique, which also dithers the loss in an MZM arm using a VOA. Using MATLAB simulations with realistic operating parameters for a silicon photonic MZM, we showed that the complex phase bias could be determined, adjusted, and maintained at any operating point even in the presence of large ($> 10\%$) complex phase drifts due to time-varying environmental fluctuations. The use of this technique was shown to improve the maximum extinction ratio of a typical modulator from about 20 dB to $\gtrsim 40$ dB and can be extended to use multiple nested MZIs for advanced modulators. The biggest trade off to using this method is that the maximum extinction ratio is limited by the dithering tones when the modulator is in the OFF state. However, using this method typically improves the extinction ratio up to that limit.

In Chapter 4, we examined the practical considerations involved to perform complex phase biasing on a fabricated silicon photonic MZM using measured data. We first explained how to implement the complex phase shifting devices using resistive heaters and PIN diodes integrated into waveguides in the MZM arms. We addressed the effects of parasitic phase shifts in the heater and PIN diode waveguides and what voltage ranges the devices need to operate within to ensure dither tones can be generated without distortion. It was shown that a VOA which only varies loss can be implemented by offsetting the parasitic phase (real part) shift of a PIN diode with the opposing phase shift of a heater. We used MATLAB to simulate the silicon MZM model from Chapter 3 considering the real device nonidealities and showed that even with the parasitic phase changes from practical devices, the complex phase

bias could be locked and maintained with errors less than 2%. We also discussed the state dependent losses of the modulator due to the Kramers-Kronig relations and how it affects the optimal complex phase bias. This chapter demonstrated that using a silicon photonic MZM for complex phase biasing is feasible.

Although this work focussed on applying the proposed complex phase biasing approach to a silicon photonic MZM, the methodology and associated performance improvements are general to MZMs in other material platforms. This work can be useful to design and control advanced MZMs on SOI or other materials for next generation optical transmitters which will use spectrally efficient modulation formats such as M-QAM which require more stringent modulator performance specifications.

5.2 Future Work

The work presented in this thesis can provide motivation for several directions of future research. First of all, the basic concept of real-time complex phase measurement and biasing should be demonstrated in a physical experiment using the fabricated PIC discussed in the previous chapter. Using the fabricated PIC and the proposed method of complex phase measurement, the effects of complex phase drift due to environmental fluctuations over time, and their effects on modulator performance can be studied. In silicon MZMs, the effect of environmental changes (e.g. ambient temperature drift) on the transfer functions of the complex phase shifting elements and the effects on biasing the complex phase should be investigated. A PIC with complex phase shifters having improved sensitivity for the dither signals as discussed in the previous chapter may be investigated to achieve accurate complex phase biasing with lower penalties than the existing PIC.

Once the concept of complex phase biasing has been demonstrated with a 1×1 MZM for digital communication purposes, the improvements and trade-offs to applying complex phase biasing to other MZI structures such as nested MZMs, filters, multi-port switches, and analog modulators can be further investigated. The topic of

real-time complex phase biasing can also be applied to other device structure topologies such as ring resonators which could allow for high extinction ratio devices for filters or modulators for example.

Appendix A

Transmission Matrix of a 2×2 MZI

A general 2×2 Mach-Zehnder Interferometer (MZI) is composed of a 2×2 coupler followed by the phase shifting arms and another 2×2 coupler. A diagram indicating these sections is shown below in Figure A.1 where A to D represent the complex field at the points labelled. The transfer matrix realization of the MZI will follow in a similar manner to that given in [77] which does not consider reflections.

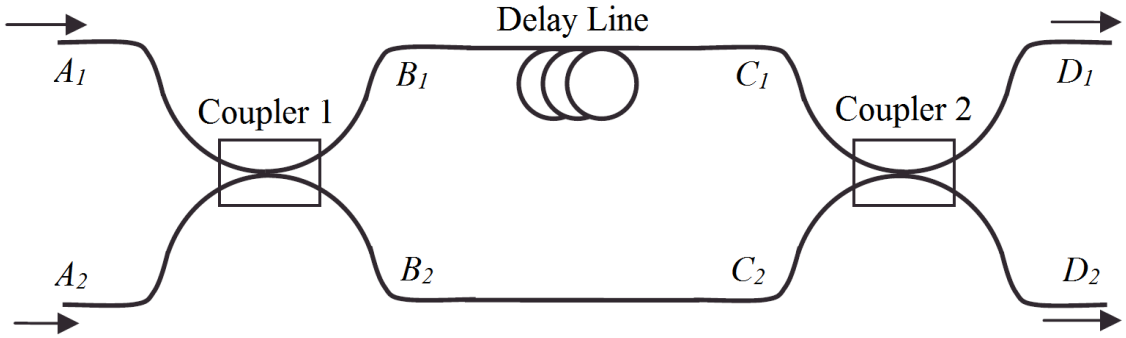

Figure A.1: Illustration of 2×2 MZI (taken from [77])

Regardless of the type of coupler used (e.g. directional coupler, multi-mode interferometer, adiabatic coupler), the transfer matrix of the first coupler can be written generally as

$$\begin{bmatrix} B_1 \\ B_2 \end{bmatrix} = \begin{bmatrix} t_{C1-11} & t_{C1-12} \\ t_{C1-21} & t_{C1-22} \end{bmatrix} \begin{bmatrix} A_1 \\ A_2 \end{bmatrix} = \mathbf{T_{C1}} \begin{bmatrix} A_1 \\ A_2 \end{bmatrix}, \tag{A.1}$$

where all elements of $\mathbf{T_{C1}}$ are complex in general. Since all passive optical elements

are reciprocal, we can further say that $t_{C1-12} = t_{C1-21}$ for all coupler types. It will be assumed that the cross-coupling losses are the same going from $A_1 \rightarrow B_2$ as $A_2 \rightarrow B_1$ and similarly that the through-coupling losses $A_1 \rightarrow B_1$ are the same as $A_2 \rightarrow B_2$. The energy conservation equation is

$$|B_1|^2 + |B_2|^2 = \left(a_{C1-t}^2 + a_{C1-\kappa}^2\right)\left(|A_1|^2 + |A_2|^2\right), \tag{A.2}$$

where a_{C1-t} and $a_{C1-\kappa}$ are the real through-port and cross-port field losses of the coupler respectively. Expanding and squaring equation A.1 yields:

$$|B_1|^2 = |t_{C1-11}|^2|A_1|^2 + |t_{C1-12}|^2|A_2|^2 + t_{C1-11}t_{C1-12}^* A_1 A_2^* + t_{C1-11}^* t_{C1-12} A_1^* A_2 \tag{A.3a}$$

$$|B_2|^2 = |t_{C1-21}|^2|A_1|^2 + |t_{C1-22}|^2|A_2|^2 + t_{C1-21}t_{C1-22}^* A_1 A_2^* + t_{C1-21}^* t_{C1-22} A_1^* A_2. \tag{A.3b}$$

Putting equation A.1 into equation A.3 gives:

$$a_{C1-t}^2 + a_{C1-\kappa}^2 = |t_{C1-11}|^2 + |t_{C1-21}|^2, \tag{A.4a}$$

$$a_{C1-t}^2 + a_{C1-\kappa}^2 = |t_{C1-12}|^2 + |t_{C1-22}|^2, \tag{A.4b}$$

and:

$$t_{C1-11}t_{C1-12}^* + t_{C1-21}t_{C1-22}^* = 0. \tag{A.5}$$

Using reciprocity ($t_{C1-12} = t_{C1-21}$) and equation A.4, it is found that $|t_{C1-11}|^2 = |t_{C1-22}|^2$. From the same equations we can define $t_{C1-11} = t_{C1-22} = a_{C1-t}$ and $t_{C1-12} = t_{C1-21} = a_{C1-\kappa}e^{-j\phi_{C1}}$ where ϕ_{C1} is found to be $-\frac{\pi}{2}$ using equation A.5. It should be obvious that $a_{C1-t}^2 + a_{C1-\kappa}^2 \leq 1$ since we are assuming the coupler is passive. It is worth mentioning in passing that the convenient value of $\phi_{C1} = -\frac{\pi}{2}$ comes from the energy conservation assumption given above in equation A.2 which simplifies equation A.4. This analysis is valid for most decent (low-loss) couplers and is used in virtually

all analysis since it applies equally well to most couplers[1]. The transfer matrix of the first and second couplers can then be written as

$$\mathbf{T_{C1}} = \begin{bmatrix} a_{C1-t} & ja_{C1-\kappa} \\ ja_{C1-\kappa} & a_{C1-t} \end{bmatrix} \tag{A.6a}$$

$$\mathbf{T_{C2}} = \begin{bmatrix} a_{C2-t} & ja_{C2-\kappa} \\ ja_{C2-\kappa} & a_{C2-t} \end{bmatrix}. \tag{A.6b}$$

The phase shifter arms section in the MZI is simply made up of two independent delay lines which can be arbitrarily unbalanced in both phase and loss. The transfer matrix relation for the phase shifter arms section is given by

$$\begin{bmatrix} C_1 \\ C_2 \end{bmatrix} = \begin{bmatrix} a_{A1}e^{-j\phi_{A1}} & 0 \\ 0 & a_{A2}e^{-j\phi_{A2}} \end{bmatrix} \begin{bmatrix} B_1 \\ B_2 \end{bmatrix} = \mathbf{T_A} \begin{bmatrix} B_1 \\ B_2 \end{bmatrix}. \tag{A.7}$$

Therefore, the total transfer matrix relation of the MZI can be written as:

$$\begin{bmatrix} D_1 \\ D_2 \end{bmatrix} = \mathbf{T_{C2}T_AT_{C1}} \begin{bmatrix} A_1 \\ A_2 \end{bmatrix} = \begin{bmatrix} t_{11} & t_{12} \\ t_{21} & t_{22} \end{bmatrix} \begin{bmatrix} A_1 \\ A_2 \end{bmatrix}. \tag{A.8}$$

In practice, only one of the input ports is excited – say A_1, while $A_2 = 0$. Furthermore, this work focusses on incoherent detection so we are only interested in the intensity transmission. The intensity transfer functions for the through and complementary ports can finally be written as

$$T_{through} = |t_{11}|^2 = \left|\frac{D_1}{A_1}\right|^2 = a_{t,1}^2 + a_{t,2}^2 - 2a_{t,1}a_{t,2}\cos(\phi), \tag{A.9a}$$

$$T_{comp} = |t_{21}|^2 = \left|\frac{D_2}{A_1}\right|^2 = a_{c,1}^2 + a_{c,2}^2 + 2a_{c,1}a_{c,2}\cos(\phi), \tag{A.9b}$$

where the definitions of $a_{t,1}$, $a_{t,2}$, $a_{c,1}$, $a_{c,2}$, and ϕ are provided in Table A.1.

[1]For the interested reader, the secondary effect of how imbalanced splitting and losses in a coupler can affect the phase difference of the complementary port are discussed in the appendix of [78]

Table A.1: MZM field loss and phase in each arm

Paremeter	Definition	Description
$a_{t,1}$	$a_{C2-t}a_{A1}a_{C1-t}$	Total field loss in arm 1 to output port D_1
$a_{t,2}$	$a_{C2-\kappa}a_{A2}a_{C1-\kappa}$	Total field loss in arm 2 to output port D_1
$a_{c,1}$	$\frac{a_{C2-\kappa}}{a_{C2-t}}a_{t,1}$	Total field loss in arm 1 to output port D_2
$a_{c,2}$	$\frac{a_{C2-t}}{a_{C2-\kappa}}a_{t,2}$	Total field loss in arm 2 to output port D_2
ϕ	$\phi_{A1} - \phi_{A2}$	Phase difference between arms in the MZI

If the second coupler is a perfect 50/50 splitter-combiner (i.e. $a_{C2-t} = a_{C2-\kappa}$), the through and complementary port transfer functions will be the same but out of phase by π (hence the name 'complementary' port) which should be obvious since all of the light can only appear at one port at a time. However, in general it cannot be assumed that the either coupler has any precise splitting ratio.

Bibliography

[1] C. Develder, M. D. Leenheer, B. Dhoedt, M. Pickavet, D. Colle, F. D. Turck, and P. Demeester. Optical networks for grid and cloud computing applications. *Proc. of IEEE*, 100(5):1149–1167, May 2012.

[2] J. Berthold, A. A. M. Saleh, L. Blair, and J. M. Simmons. Optical networking: past, present and future. *IEEE J. Light. Tech.*, 29(9):1104–1118, May 2008.

[3] E. Ip, P. Ji, E. Mateo, Y. K. Huang, L. Xu, D. Qian, N. Bai, and T. Wang. 100G and beyond transmission technologies for evolving optical networks and relevant physical-layer issues. *Proc. of IEEE*, 100(5):1065–1078, May 2012.

[4] J. Capmany and D. Novak. Microwave photonics combines two worlds. *Nature Photonics*, 1:319–330, June 2007.

[5] J. Yao. A tutorial on microwave photonics. *IEEE J. Light. Tech*, 27(3):314–335, February 2009.

[6] A. V. Krishnamoorthy, R. Ho, X. Zheng, H. Schwetman, J. Lexau, P. Koka, G. Li, I. Shubin, and J. E. Cunningham. Computer systems based on silicon photonics interconnects. *Proc. of IEEE*, 97(7):1337–1361, July 2009.

[7] M. K. Smit and C. V. Dam. PHASAR-based WDM-devices: principles, design and applications. *IEEE J. Sel. Topics Quantum Electron.*, 2(2):236–250, June 1996.

[8] J. Broukaert, W. Bogaerts, S. Selvaraja, P. Dumon, R. Baets, and D. V.

Thourhout. Planar concave grating demultiplexer with high reflective Bragg reflector facets. *IEEE Photonics Tech. Lett.*, 20(4):309–311, February 2008.

[9] M. Kuznetsov. Cascaded coupler Mach-Zehnder channel dropping filters for wavelength-division-multiplexed optical systems. *J. Light. Tech.*, 12(2):226–230, February 1994.

[10] Q. Xu, B. Schmidt, J. Shakya, and M. Lipson. Cascaded silicon micro-ring modulators for WDM optical interconnection. *Opt. Express*, 14(20):9431–9435, October 2006.

[11] G. P. Agrawal. *Fiber-optic communication systems*. Wiley, 4 edition, 2010.

[12] R. Soref. The past, present, and future of silicon photonics. *IEEE J. Sel. Quantum Electron.*, 12(6):1678–1687, December 2006.

[13] T. Baehr-Jones, R. Ding, A. Ayazi, T. Pinguet, M. Streshinsky, N. Harris, J. Li, L. He, M. Gould, Y. Zhang, A. E. J. Lim, T. Y. Liow, S. H. G. Teo, G. Q. Lo, and M. Hochberg. A 25 Gb/s silicon photonics platform. *arXiv:1203.0767*, March 2012. Retrieved from: `http://arxiv.org/abs/1203.0767v1`, accessed: 2013-12-10.

[14] R. A. Soref and B. R. Bennett. Electrooptical effects in silicon. *IEEE J. Quantum Electron.*, 23(1):123–129, January 1987.

[15] A. Liu, L. Liao, D. Rubin, H. Nguyen, B. Ciftcioglu, Y. Chetrit, N. Izhaky, and M. Paniccia. High-speed optical modulation based on carrier depletion in a silicon waveguide. *Opt. Express*, 15(2):660–668, January 2007.

[16] W. M. J. Green, M. J. Rooks, L. Sekaric, and Y. A. Vlasov. Ultra-compact, low RF power, 10 Gb/s silicon Mach-Zehnder modulator. *Opt. Express*, 15(25):17106–17113, December 2007.

[17] T. Y. Liow, J. Song, X. Tu, A. E. J. Lim, Q. Fang, N. Duan, M. Yu, and G. Q. Lo.

Silicon optical interconnect device technologies for 40 Gb/s and beyond. *IEEE J. Sel. Quant. Electron.*, 19(2), April 2013.

[18] M. R. Watts, W. Z. Zortman, D. C. Trotter, R. W. Young, and A. L. Lentine. Low-voltage, compact, depletion-mode, silicon Mach-Zehnder modulator. *IEEE J. Sel. Topics Quantum Electron.*, 16(1):159–164, February 2010.

[19] E. I. Ackerman. Broad-band linearization of a Mach-Zehnder electrooptic modulator. *IEEE Trans. Microwave Theory Tech.*, 47(12):2271–2279, December 1999.

[20] A. Liu, L. Liao, D. Rubin, J. Basak, Y. Chetrit, H. Nguyen, D. W. Kim, A. Barkai, R. Jones, N. Elek, R. Cohen, N. Izhaky, and M. Paniccia. Silicon photonic integration for high-speed applications. In *SPIE Proceedings*, volume 6898, San Jose, USA, January 2008.

[21] A. Chen and E. J. Murphy, editors. *Broadband Optical Modulators: Science Technology, and Applications*, chapter 15: Bias control techniques. CRC Press, 2012.

[22] K. Padmaraju, J. Chan, L. Chen, M. Lipson, and K. Bergman. Thermal stabilization of a microring modulator using feedback control. *Opt. Express*, 29(27):27999–28008, December 2012.

[23] J. Komma, C. Schwarz, G. Hofmann, D. Heinert, and R. Nawrodt. Thermo-optic coefficient of silicon at 1550 nm and cryogenetic temperatures. *Apply. Phys. Lett.*, 101(4):041905 – 041905–4, July 2012.

[24] S. Gronbach. Method and apparatus for controlling a bias voltage of a Mach-Zehnder modulator. US Patent 7 075 695 B2, Lucent Technologies Inc., Murray Hill, NJ (US), July 2006.

[25] Bias control for external modulators used in digital data transmission applications. Application note, JDSU, 2008.

[26] L.L. Wang and T. Kowalcyzk. A versatile bias control technique for any-point locking in lithium niobate Mach-Zehnder modulators. *J. Light. Tech.*, 28(11):1703–1706, June 2010.

[27] T. Kawanishi, T. Sakamoto, A. Chiba, and M. Izutsu. Study of precise optical modulation using Mach-Zehnder interferometers for advanced modulation formats. In *European Conf. of Optical Comm. (ECOC)*, Berlin, Germany, September 2007.

[28] H. Kim and A. H. Gnauck. Chirp characteristics of dual-drive Mach-Zehnder modulator with a finite DC extinction ratio. *IEEE Photonics Tech. Lett.*, 14(3):298–300, March 2002.

[29] A. H. Gnauck, S. K. Korotky, J. J. Veselka, J. Nagel, C. T. Kemmerer, W. J. Minford, and D. T. Moser. Dispersion penalty reduction using an optical modulator with adjustable chirp. *IEEE Photonics Tech. Lett.*, 3(10):916–918, October 1991.

[30] T. Kawanishi. Precise and high-speed control of light for advanced modulation formats. In *OptoElec. and Comm. Conf. (OECC)*, pages 560–561, Sapporo, Japan, September 2010.

[31] T. Kawanishi, T. Sakamoto, M. Tsuchiya, and M. Izutsu. 70dB extinction-ratio $LiNbO_3$ optical intensity modulator for two-tone lightwave generation. In *Optical Fiber Comm. Conf. (OFC)*, Anaheim, USA.

[32] Y. Ogiso, Y. Tsuchiya, S. Shinada, S. Nakajima, T. Kawanishi, and H. Nakajima. High extinction-ratio integrated Mach-Zehnder modulator with active Y-branch for optical SSB signal generation. *IEEE Photonics Tech. Lett.*, 22(12):941–943, June 2010.

[33] Y. Zhang, S. Yang, A. E. J. Lim, G. Q. Lo, C. Galland, T. Baehr-Jones, and M. Hochberg. A compact and low loss Y-junction for submicron silicon waveguide. *Opt. Express*, 21(1):1310–1316, January 2013.

[34] D. J. Thomson, Y. Hu, G. T. Reed, and J. M. Fedeli. Low loss MMI couplers for high performance MZI modulators. *IEEE Photonics Tech. Lett.*, 22(20):1485–1487, October 2010.

[35] K. Solehmainen, M. Kapulainen, M. Harjanne, and T. Aalto. Adiabatic and multimode interference couplers on silicon-on-insulator. *IEEE Photonics Tech. Lett.*, 18(21):2287–2289, November 2006.

[36] H. Yun, W. Shi, Y. Wang, L. Chrostowski, and A. F. Jaeger. 2×2 adiabatic 3-dB coupler on silicon-on-insulator rib waveguides. In *Proc. SPIE, Photonics North*, Ottawa, Canada, June 2013.

[37] 40 GHz phase and intensity modulators. Catalog v21, ThorLabs. Retrieved from: `http://www.thorlabs.com/catalogpages/V21/1205.PDF`, accessed: 2013-12-10.

[38] P. J. Winzer and R. J. Essiambre. Advanced optical modulation formats. *Proc. of IEEE*, 94(5):952–985, May 2006.

[39] I. P. Kaminow, T. Li, and A. E. Willner, editors. *Optical fiber telecommunications: Systems and networks*. Academic Press, VIB edition, 2013.

[40] K. P. Ho and H. W. Cuei. Generation of arbitrary quadrature signals using one dual-drive modulator. *J. Light. Tech*, 23(2):764–770, February 2005.

[41] Extinction ratio and power penalty. Application Note HFAN-2.2.0, Maxim Integrated, April 2008.

[42] F. Koyama and K. Iga. Frequency chirping in external modulators. *J. Light. Tech*, 6(1):87–93, January 1988.

[43] S. K. Kim, O. Mizuhara, Y. K. Park, L. D. Tzeng, Y. S. Kim, and J. Jeong. Theoretical and experimental study of 10 Gb/s transmission performance using 1.55 μm $LiNbO_3$-based transmitters with adjustable extinction ratio and chirp. *J. Light. Tech.*, 17(8):1320–1325, August 1999.

[44] J. Jeong and Y. K. Park. Accurate determination of transient chirp parameters in high speed digital lightwave transmitters. *Electron. Lett.*, 33(7):605–606, March 1997.

[45] J. Leuthold, P. A. Besse, J. Eckner, E. Gamper, M. Dülk, and H. Melchior. All-optical space switches with gain and principally ideal extinction ratios. *IEEE J. Quantum Electron.*, 34(4):622–633, April 1998.

[46] B. Razavi. *Design of integrated ciruits for optical communications*, chapter 2: Basic concepts. McGraw Hill, 2002.

[47] C. H. Cox and E. I. Ackerman. Modulator bias control. US Patent 7 369 290 B1, Photonic Systems, Inc., Burlington, MA (US), May 2008.

[48] Y. Li, Y. Zhang, and Y. Huang. Slope value detection-based ditherless bias control technique for Mach-Zehnder modulator. *Opt. Engineering*, 52(8), August 2013.

[49] NRZ bandwidth: LF cutoff and baseline wander. Application Note HFAN-09.0.4, Maxim Integrated, April 2008.

[50] Z. Huang, X. Zhang, S. Zheng, X. Jin, and H. Chi. Any bias point control of Mach-Zehnder electro-optic modulator and its applications in optimization of radio-over-fiber links. In *Proc. of IEEE*, Microwave Photonics (MWP), pages 218–221, October 2011.

[51] A. Novack, Y. Liu, R. Ding, M. Gould, T. Baehr-Jones, Q. Li, Y. Yang, Y. Ma, Y. Zhang, K. Padmaraju, K. Bergman, A. E. J. Lim, G. Q. Lo, and M. Hochberg. A 30 GHz silicon photonic platform. In *Proc. SPIE, Integrated optics: physics and simulations*, Prague, Czech Republic, May 2013.

[52] AD7663. Datasheet Rev. B, Analog Devices, 2003.

[53] G. Ghione. *Semiconductor devices for high-speed optoelectronics*, chapter 6: Modulators. Cambridge University Press, 2009.

[54] H. Kawakami, E. Yoshida, and Y. Miyamoto. Asymmetric dithering techniques for bias condition monitoring in optical QPSK modulator. *Electron. Lett.*, 46(6):430–431, March 2010.

[55] H. Kawakami, E. Yoshida, and Y. Miyamoto. Auto bias control technique based on asymmetric bias dithering for optical QPSK modulation. *J. Light. Tech.*, 30(7):962–968, April 2012.

[56] H. Kawakami, T. Kobayashi, E. Yoshida, and Y. Miyamoto. Auto bias control technique for optical 16-QAM transmitter with asymmetric bias dithering. *Opt. Express*, 19(26):308–312, November 2011.

[57] T. Y. Liow, K. W. Ang, Q. Fang, J. F. Song, Y. Z. Xiong, M. B. Yu, G. Q. Lo, and D. L. Kwong. Silicon modulators and germanium photodetectors on SOI: monolithic integration, compatibility, and performance optimization. *IEEE J. Sel. Quant. Electron.*, 16(1):307–315, February 2010.

[58] Photonics multiple project wafer prototyping. Foundry service specifications, A*STAR IME. Retrieved from: `http://www.ime.a-star.edu.sg/research_page/photonics_multiple_project_wafer__mpw__prototyping`, accessed: 2013-12-10.

[59] A. Yariv and P. Yeh. *Photonics: optical electronics in modern communications*. Oxford University Press, 6 edition, 2006.

[60] T. Baehr-Jones, R. Ding, Y. Liu, A. Ayazi, T. Pinguet, N. C. Harris, M. Streshinsky, P. Lee, Y. Zhang, A. E. J. Lim, T. Y. Liow, S. H. G. Teo, G. Q. Lo, and M. Hochberg. Ultralow drive voltage silicon traveling-wave modulator. *Opt. Express*, 20(11):12014–12020, May 2012.

[61] L. Liao, A. Liu, D. Rubin, J. Basak., Y. Chetrit, H. Nguyen, R. Cohen, N. Izhaky, and M. Paniccia. 40 Gbit/s silicon optical modulator for high-speed applications. *Electron. Lett.*, 43(22), October 2007.

[62] D. J. Thomson, F. Y. Gardes, Y. Hu, G. Mashanovich, M. Fournier, P. Grosse, J. M. Fedeli, and G. T. Reed. High contrast 40Gbit/s optical modulation in silicon. *Opt. Express*, 19(12):11507–11516, May 2011.

[63] D. J. Thomson, F. Y. Gardes J. M. Fedeli, S. Zlatanovic, Y. Hu, B. P. P. Kuo, E. Myslivets, N. Alic, S. Radic, G. Z. Mashanovich, and G. T. Reed. 50-Gb/s silicon optical modulator. *IEEE Photonics Tech. Lett.*, 24(4):234–236, February 2012.

[64] H. Jayatilleka, W. D. Sacher, and J. K. S. Poon. Analytical model and fringing-field parasitics of carrier-depletion silicon-on-insulator optical modulation diodes. *IEEE Photon. J.*, 5(1), February 2013.

[65] L. Chrostowski and M. Hochberg. *Silicon photonics design.* 2013. Retrieved from: `https://www.dropbox.com/sh/dpld0btk29psdbi/8ZUuK3Di0S/book_ipad_h.pdf`, accessed: 2013-12-10.

[66] G. Ghione and C. Naldi. Analytical formulas for coplanar lines in hybrid and monolithic MICs. *Electron. Lett.*, 20(4):179–181, February 1984.

[67] M. L. Kao and Y. K. Park. Basic parameters of coplanar-strip waveguides on multilayer dielectric/semiconductor substrates, part 2: low permittivity superstrates. Application note, IEEE Microwave Magazine, September 2003.

[68] M. A. Popović. Resonant optical modulators beyond conventional energy-efficiency and modulation frequency limitations. In *Nanocavities and Nanoresonators (IMC)*, Monterey, United States, July 2010.

[69] W. D. Sacher, W. M. J. Green, S. Assefa, T. Barwicz, S. M. Shank, Y. A. Vlasov, and J. K. S. Poon. Controlled coupling in silicon microrings for high-speed, high extinction ratio, and low-chirp modulation. In *Conf. of Lasers and Electro-optics (CLEO)*, Baltimore, United States, May 2011.

[70] T. Baba, S. Akiyama, M. Imai, N. Hirayama, H. Takahashi, Y. Noguchi, T. Horikawa, and T. Usuki. 50-Gb/s ring-resonator-based silicon modulator. *Opt. Express*, 21(10):11869–11876, May 2013.

[71] W. D. Sacher, W. M. J. Green, S. Assefa, T. Barwicz, H. Pan, S. M. Shank, Y. A. Vlasov, and J. K. S. Poon. Coupling modulation of microrings at rates beyond the linewidth limit. *Opt. Express*, 21(8):9722–9733, April 2013.

[72] A. Yariv. Universal relations for coupling of optical power between microresonators and dielectric waveguides. *Electron. Lett.*, 36(4):321–322, February 2000.

[73] J. C. Mikkelsen, W. D. Sacher, and J. K. S. Poon. Adiabatically widened silicon microring resonators with improved tolerance to wafer-scale variations. In *Optical Fiber Comm. Conf. (OFC)*, San Fransisco, United States, March 2014.

[74] J. M. Choi, R. K. Lee, and A. Yariv. Control of critical coupling in a ring resonator-fiber configuration: application to wavelength-selective switching, modulation, amplification, and oscillation. *Opt. Lett.*, 26(16):1236–1238, August 2001.

[75] D. G. Rabus, M. Hamacher, U. Troppenz, and H. Heidrich. High-Q channel-dropping filters using ring resonators with integrated SOAs. *IEEE Photon. Tech. Lett.*, 14(10):1442–1444, October 2002.

[76] V. M. Menon, W. Tong, and S. R. Forrest. Control of quality factor and critical coupling in microring resonators through integration of semiconductor optical amplifier. *IEEE Photon. Tech. Lett.*, 16(5):1343–1345, May 2004.

[77] R. Hui and M. O'Sullivan. *Fiber optic measurement techniques*, chapter 2: Basic Instrumentation for Optical Measurement, pages 160–164. Academic Press, 2008.

[78] G. L. Abbas, V. W. S. Chan, and T. K. Yee. A dual-detector optical heterodyne receiver for local oscillator noise suppresion. *J. Light. Tech.*, 3(5):1110–1122, October 1985.